

A dissymmetric [Gd₂] coordination molecular dimer hosting six addressable spin qubits

Fernando Luis,^{1,2,*} Pablo J. Alonso,^{1,2} Olivier Roubeau,^{1,2} Verónica Velasco,³ David Zueco,^{1,2,4} David Aguilà,³ Leoní A. Barrios,³ Guillem Aromí^{3,*}

¹ Instituto de Ciencia de Materiales de Aragón (ICMA), CSIC and Universidad de Zaragoza, Plaza San Francisco s/n, 50009 Zaragoza, Spain.

² Dpto. de Física de la Materia Condensada, Universidad de Zaragoza, Pedro Cerbuna 12, 50009 Zaragoza, Spain

³ Departament de Química Inorgànica and IN2UB, Universitat de Barcelona, Diagonal 645, 08028 Barcelona, Spain

⁴ Fundación ARAID, Av. de Ranillas 1-D, 50018 Zaragoza, Spain

Email: fluis@unizar.es, guillem.aromi@qi.ub.edu

Abstract

Artificial magnetic molecules are suitable hosts to one or several spin qubits, which could then implement small-scale algorithms. In order to become of practical use, such molecular spin processors need to increase the dimension d of the available computational space and fulfill the highly demanding conditions that warrant universal operations. Here, we design, synthesize and fully characterize dissymmetric molecular dimers hosting either one or two Gd(III) ions. The strong sensitivity of Gd(III) magnetic anisotropy to the symmetry of its local coordination gives rise to different zero-field splittings at each coordination site. As a result, the [LaGd] and [GdLu] complexes provide realizations of distinct $d = 8$ spin qudits, whereas the [Gd₂] dimer meets all requirements, including a complete set of operations, to act as a $d = 64$ all-electron spin qudit (or, equivalently, as six addressable qubits). Electron paramagnetic resonance experiments show that the relevant resonant transitions between different spin states can be coherently controlled, with coherence times T_M of the order of 1 μ s limited by intramolecular hyperfine interactions. Coordination complexes with embedded quantum functionalities are promising building blocks for quantum computation and simulation hybrid platforms.

Keywords: Molecular magnets, spin qubits and qudits, quantum spin coherence, quantum computation and simulation.

Introduction

Electronic spins in solids are natural candidates to encode qubits, the basic units of future quantum computers.¹ Quantized spin projections give rise to a discrete set of states that can be coherently manipulated by external magnetic field pulses. In addition, they are insensitive to electric noise and can therefore show longer coherence times than qubits based on electric (e.g. superconducting) circuits. Outstanding examples are magnetic defects in semiconductor hosts, such as NV⁻ centres in diamond² or P⁺ donors in silicon.³ These systems are however not easy to tune, and wiring them up into a scalable architecture remains very challenging. A promising alternative to address these questions relies on the use of electron spins hosted by artificial molecules, *i.e.* organic radicals or transition-metal complexes.⁴⁻⁶ This chemistry-based approach affords the synthesis of macroscopic numbers of identical qubits. The design of the metal coordination provides some control over the spin levels, which determine the qubit frequencies.^{7,8} Furthermore, the spin coherence can be enhanced by either reducing the number of neighbouring nuclear spins or by engineering qubit states that are insensitive to magnetic field fluctuations. As a result, molecular spin qubit coherence times T_M have shown very significant improvements over the past years.⁸⁻¹³

But arguably the most appealing trait of this approach is that it offers the possibility of scaling up computational resources within each molecular unit. The most straightforward strategy is to incorporate several (two or more) magnetic centres, each of them realizing a qubit. Several spin carriers can be assembled in a rational way, such that their nature, disposition and interaction result in a set of addressable transitions that allow coherently manipulating all qubit states.⁶ At the synthetic level, this implies a necessary dissymmetry between the different magnetic centres. Early successful examples in either homometallic^{14,15} or heterometallic^{16,17} lanthanide dimers have shown that conditions to realize both CNOT and $\sqrt{\text{SWAP}}$ two-qubit gates can be fulfilled,¹⁸ and allowed measuring the quantum coherence of a CNOT gate with T_M of about 400 ns.¹⁹⁻²¹ Also, modular supramolecular approaches able to incorporate multiple weakly coupled Cr₇Ni qubits have been developed²² and used to implement C-PHASE two-qubit gates.²³ A second strategy is to profit from the internal spin levels of each magnetic centre to create d -dimensional ($d > 2$) quantum systems, that is, qudits. Examples include the coherent manipulation of the multiple nuclear spin states of ¹⁵⁹TbPC₂ ($I = 3/2$, $d = 4$),^{24,25} Et₄N[¹⁶³DyPC₂] ($I = 5/2$, $d = 6$)²⁶ and ¹⁷³Yb(trensol) ($I = 5/2$, $d = 6$)²⁷ mononuclear complexes. The former of these enabled a first realization of a three-level Grover quantum search algorithm in a single molecule, using tools of molecular electronics to read-out the qudit state.²⁸ Electronic spin qudits can also be realized in some cases, for instance by using the $S = 7/2$ spin manifold of a Gd(III) ion provided that it has a sufficiently low magnetic anisotropy to make all levels experimentally accessible.²⁹

The integration of multiple levels in well-defined complexes increases the density of quantum information handled by these systems and could allow embedding specific functionalities, say quantum error correction or some simple quantum algorithms and

simulations,^{27,30-32} at the molecular scale. These applications demand increasing the dimension of the computational space beyond three qubits while retaining the ability to perform universal quantum operations.^{30,33} Meeting both conditions in a molecule still represents a daunting challenge.

Here we show that it is possible to design and synthesize such building blocks via the combination of the two strategies outlined above. The rational design of a coordination complex with multiple and distinctive Gd(III) ions would allow to scale up to 6 or more addressable qubits within one single molecule, with the potential of realizing different quantum gate operations. We focus here on the realization of this scaling-up in a dissymmetric [Gd₂] molecule in which the two Gd(III) ions have a slightly different coordination.^{14,15} The isolated properties of each Gd(III) $d = 8$ qudit are first determined through the isolation and study of the [LaGd] and [GdLu] analogue molecules, in which the Gd(III) ions occupy either of the two coordination sites present in [Gd₂]. The results show that the [Gd₂] molecule holds the promise to act as a 6-qubit quantum processor or as a $d = 64$ electronic spin qudit.

Results

Synthesis and structures

We previously showed that the ligand H₃L forms a series of dissymmetric homometallic dilanthanide complexes of formula (Hpy)[Ln₂(HL)₃(NO₃)(py)(H₂O)] (H₃L = 6-(3-oxo-3-(2-hydroxyphenyl)propionyl)-pyridine-2-carboxylic acid, py = pyridine), among which the [Gd₂] compound studied here.^{14,15} The two different Ln environments resulting from the different coordination pockets created by the three deprotonated HL²⁻ ligands and their disposition give rise to two metal sites with markedly different Ln-O and Ln-N bond lengths, one position being systematically larger than the other. This allows forming in a controlled manner heterometallic dilanthanide molecules, provided their ionic radii are sufficiently different.^{16,17,34} This unique synthetic strategy was first used to isolate the [CeEr], [LaEr] and [CeY] analogues.¹⁹ Here, in order to study each Gd(III) ion present in [Gd₂], albeit isolated from each other, the [LaGd] and [GdLu] analogues are prepared in a similar manner. Note that the differences in ionic radii Δr_i , respectively of 9.4 and 7.7 pm,³⁴ are sufficient to expect the formation of a homogeneous heterometallic single phase.^{16,17} Thus, equimolar amounts of Gd(NO₃)₃ and either La(NO₃)₃ or Lu(NO₃)₃ were made react with H₃L in pyridine. Layering of the resulting clear yellow solution with Et₂O resulted in homogeneous phases of yellow crystals that were found by single-crystal x-ray diffraction to consist of (Hpy)[LaGd(HL)₃(NO₃)(py)(H₂O)]·5py ([LaGd]) and (Hpy)[GdLu(HL)₃(NO₃)(py)(H₂O)]·5py ([GdLu]).

Compounds [LaGd] and [GdLu] crystallize in the monoclinic space group $P2_1/n$, with the asymmetric unit coinciding with their formula and $Z = 4$. The pyridinium cation forms a hydrogen bond with one of the carboxylic oxygen atoms from one of the HL²⁻ ligands. Two of the five lattice pyridine molecules are hydrogen bonded to the coordinated water molecule (Fig S1). The metal complexes (Fig. 1) show the structure observed consistently within this series of compounds, with two lanthanide ions bridged and

chelated by three HL²⁻ ligands in two opposite orientations with respect to the La...Gd or Gd...Lu vector. Thus two different coordination environments are present, with two/one (O,N,O) pocket and one/two (O,O) chelates respectively for site 1/2. The coordination sphere is completed by a nitrate ion on site 1 (La in **[LaGd]** and Gd in **[GdLu]**), and by one pyridine molecule and a water molecule on site 2 (Gd in **[LaGd]** and Lu in **[GdLu]**). In **[LaGd]**, the coordinated nitrate is bidentate, resulting in a coordination number CN of 10 for the larger La(III) ion, while the rest have CN of 9. The intermetallic separations are respectively 3.8941(3) and 3.761(1) Å for La...Gd and Gd...Lu, to be compared with the intermediate 3.804(1) Å Gd...Gd separation in **[Gd₂]**. The average Ln–O bonds to HL²⁻ donors are longer at site 1, 2.544 Å (La in **[LaGd]**) and 2.432 Å (Gd in **[GdLu]**), than at site 2, 2.405 Å (Gd in **[LaGd]**) and 2.342 Å (Lu in **[GdLu]**). The differences ΔO between both sites are thus respectively 0.139 and 0.090 Å, larger than those observed in the homometallic analogues [La₂] (ΔO=0.045 Å) and [Gd₂] (ΔO=0.026 Å),¹⁴ an indication that the lanthanide ions have taken selectively the optimal relative positions following their respective ionic radii.^{16,17}

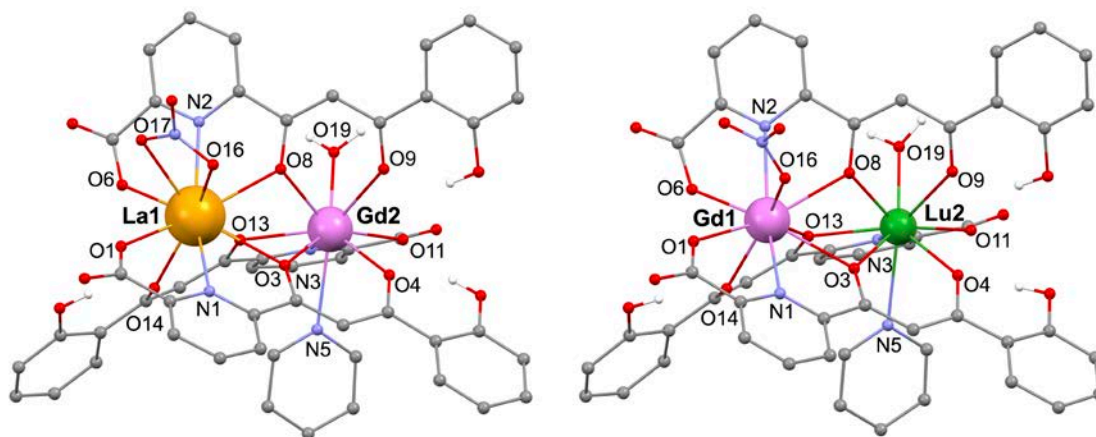


Figure 1. Molecular structures of [LaGd] and [GdLu] spin quidits. For clarity, hydrogens not involved in H-bonding and lattice pyridine molecules are omitted. Atomic sites involved in the coordination labelled. Colour code: O, red; N, light blue; C, grey.

The coordination sphere at both Gd sites also differ in shape, as indicated by continuous shape measures (Fig. S2).^{35,36} Thus, the Gd2 site in **[LaGd]** is closest to an ideal capped antiprism (C_{4v} symmetry) and to an ideal tricapped trigonal prism (D_{3h} symmetry). The Gd1 site in **[GdLu]** is more irregular as indicated by distances to any ideal polyhedron 3-4 times larger. These differences are identical to those found between the two Gd sites in **[Gd₂]**. The metal site composition is confirmed by the unreasonable relative displacement parameters and worse final refinement obtained for any other distribution of metals within the molecular structure.

The molecular metal composition observed in the solid-state is confirmed by Electrospray Ionization Mass Spectrometry (ESI-MS), which also allows ensuring the integrity of the molecular structure in solution. Thus, the spectra obtained from solutions of **[LaGd]**, **[Gd₂]** and **[GdLu]** each exhibit a prominent peak with respectively m/z of 1146.98, 1166.01 and 1183.02 and isotopic distribution that agree with the

corresponding $[\text{LnLn}'(\text{H}_2\text{L})(\text{HL})_2]^+$ fragment. For **[LaGd]** and **[GdLu]**, peaks corresponding to the homometallic fragments are also detected, indicating a process of partial scrambling occurs in solution. This is however very limited and follows the relative Δr_i , in line with previous ESI-MS and density functional theory studies.^{16,17} Overall, the heterometallic molecular composition seen in the solid-state structure is maintained in solution, which is relevant for the studies of coherent spin dynamics done on diluted solutions (see below).

Isolated qubits in **[LaGd]** and **[GdLu]**: magnetic dissymmetry

A crucial requirement to properly define a qudit, or n qubits, using a system with multiple energy levels $d = 2^n$ is that the energy spectrum has some nonlinearity, *i.e.* that the levels are not simply equidistant as those of a harmonic oscillator.³⁰ In the case of Gd(III), with its ground state $S = 7/2$, this condition relies on the existence of a finite magnetic anisotropy.^{7,29} An advantage of this ion is that, because of its $L = 0$ configuration, the intrinsic anisotropy of the free ion is negligible. Any zero-field splitting of the $d = 8$ spin levels necessarily arises from small distortions that the coordination environment induces on the close to spherical 4f electronic shell. This property makes Gd(III) a kind of model crystal field probe and allows modifying the magnetic anisotropy via changes in the local coordination. Often, this anisotropy is also quite small, much smaller than those typically found for other lanthanides with $L \neq 0$,^{4,5,37-39} thereby making these levels accessible via conventional magnetic spectroscopy techniques.

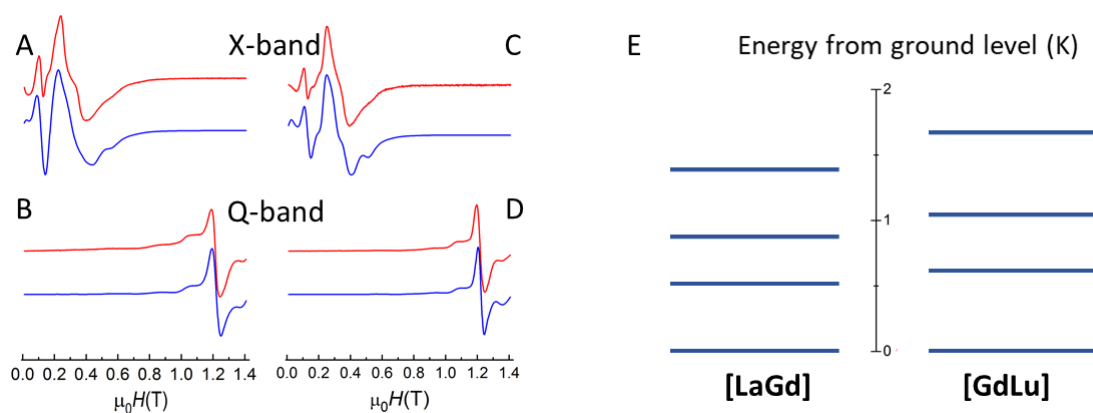


Figure 2. Magnetic spectroscopy of **[LaGd] and **[GdLu]** spin qudits.** X-band and Q-band continuous wave EPR spectra measured on powdered samples of **[LaGd]** (A and B) and of **[GdLu]** (C and D) at $T = 6$ K. The red solid lines are experimental data, whereas the blue solid lines are simulations obtained with the spin Hamiltonian (1) and the parameters given in the text. Panel E compares the zero-field splitting of the Gd(III) spin ground state in both molecules, obtained using the parameters extracted from the simulations, corresponding to the coordination sites 1 and 2 in the structures of Fig. 1.

The continuous-wave Electron Paramagnetic Resonance (cw-EPR) spectra of **[LaGd]** and **[GdLu]** are shown in Fig. 2. The experiments have been performed on powdered samples using both X-band (frequency $\omega/2\pi = 9.886$ GHz) and Q-band ($\omega/2\pi = 33.33$ GHz)

cavities. Spectra measured on each sample at different frequencies do not simply scale as a function of H/ω , where H is the external magnetic field. This shows already that Gd(III) acquires a net magnetic anisotropy in the two possible coordination sites 1 and 2 (Fig. 1). Besides, the spectra of the two samples are also different, thus showing that the magnetic anisotropy depends on the coordination environment (Fig. 2E).

In order to render these arguments quantitative, we have performed fits of the experimental spectra using the EPR simulation package EasySpin.⁴⁰ Taking into account the low symmetry of the Gd coordination sites in these molecules, we have considered the simplest lowest-order spin Hamiltonian

$$\mathcal{H} = -DS_z^2 + E(S_x^2 - S_y^2) - g\mu_B\vec{H}\vec{S} \quad (1)$$

where D and E are the anisotropy constants and g is the gyromagnetic factor. Results of these fits are compared to the experimental results in Fig. 2. A reasonably good agreement was obtained by setting $D/k_B = 0.096$ K, $E/k_B = -0.032$ K and $g = 1.99$ for **[LaGd]** and $D/k_B = 0.115$ K, $|E|/k_B = 0.038$ K and $g = 1.99$ for **[GdLu]**. The line broadenings suggest that there is sizeable distribution in D and E , of about 60% for both compounds.

Another experimental technique that provides information on the structure of electronic energy levels is heat capacity. Results obtained for the two molecular “monomers” are shown in Fig. 3. Above 10 K, the specific heat c_p/R is dominated by excitations of vibrational modes. This lattice contribution has been measured directly on the diamagnetic derivative [YLa],¹⁹ and agrees very well with the high temperature behaviour. The additional anomaly observed, at $H = 0$, for both **[LaGd]** and **[GdLu]** below 2 K must then be associated with the finite splitting of the Gd(III) electronic spin levels. A nice feature of these results is that the position of the specific heat maximum provides a direct measure of the overall zero-field splitting.⁴¹

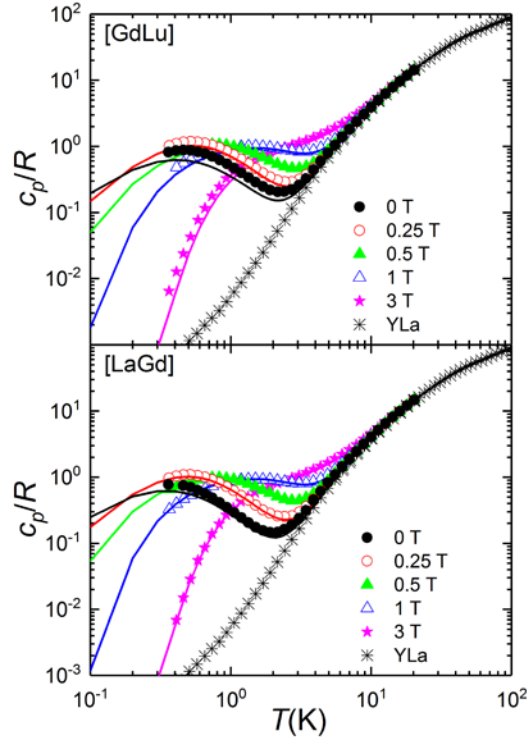


Figure 3. Field-dependent specific heat of [GdLu] and [LaGd] spin qudits. Curves were measured at zero and different applied magnetic fields on powdered samples of **[GdLu]** (top) and **[LaGd]** (bottom). Data measured for the diamagnetic complex [YLa],¹⁹ which arise from vibrational excitations only, are also shown in both panels. The solid lines are numerical calculations of the magnetic heat capacity, derived from Eq. (1) with the same parameters, and their distributions, used to account for the cw-EPR data of Fig. 2 to which this nonmagnetic contribution has been added.

The comparison between results measured for **[LaGd]** and **[GdLu]** confirms that the magnetic anisotropy is slightly stronger for the latter. This Schottky-like broad maximum is indeed well accounted for by numerical calculations based on Eq. (1) using the same magnetic anisotropy parameters D and E derived from EPR experiments (and with the same D - and E - strains). A good agreement is also found for data measured under non-zero magnetic fields. Results for the two compounds become progressively closer to each other as H increases, due to the relatively weak magnetic anisotropy of Gd(III) and to the predominance of the Zeeman term in Eq. (1) for sufficiently strong H .

In conclusion, the results shown in this section demonstrate that Gd(III) ions coordinated in the molecular structures of **[LaGd]** and **[GdLu]** have low-lying electronic energy level spectra that provide basis for two different spin qudits.

Exchange coupling in [Gd₂]

In this section, we turn our attention to the molecular dimer **[Gd₂]**. This complex hosts the two magnetic ions, in different coordination sites, whose properties in isolation have been discussed in the previous section. From this discussion, it would seem that this molecule, with $(2S+1) \times (2S+1) = 64 = 2^6$ unequally spaced levels, provides a proper implementation of a $d = 64$ qudit or of six qubits. However, an additional necessary

ingredient, related with the condition of universality that we discuss below, is the existence of a net coupling between the two spins.

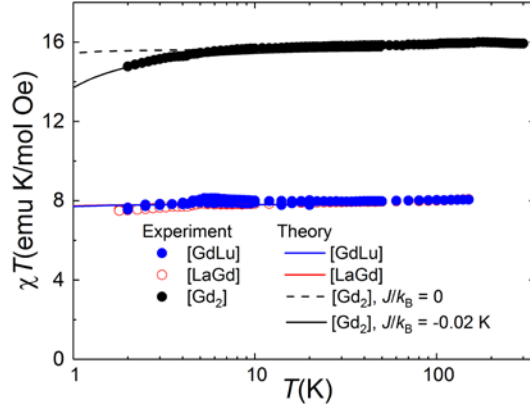


Figure 4. Magnetic coupling in the [Gd₂] dimer. Product of the molar susceptibility χ times temperature measured on powder samples of [LaGd], [GdLu] and [Gd₂]. The lines are numerical calculations. In the case of the molecules hosting only one magnetic ions, they are derived from the spin Hamiltonian (1) with the anisotropy parameters determined independently from EPR experiments (Fig. 2). In the case of [Gd₂], the calculations include also a spin-spin coupling, as in Eq. (2), with two values for the coupling constant J .

In order to get information of the spin-spin interaction within the molecule, we have compared the magnetic, spectroscopic and thermal properties of the [Gd₂] complex with those measured on [LaGd] and [GdLu]. Figure 4 shows the magnetic response of the three samples. While the χT plots of [LaGd] and [GdLu] agree with the predictions for isolated Gd(III) ions (an almost temperature independent value, in agreement with Curie's law), the data for [Gd₂] show a decrease below approximately 4 K. This behaviour is compatible with the existence of a weak isotropic coupling described by the following spin Hamiltonian

$$\mathcal{H} = \mathcal{H}_1 + \mathcal{H}_2 - J\vec{S}_1\vec{S}_2 \quad (2)$$

where \mathcal{H}_1 and \mathcal{H}_2 are the spin Hamiltonians of each isolated Gd(III) ion, given by Eq. (1) with the appropriate parameters, and J is the spin-spin coupling constant. As a further simplification, the anisotropy axes at sites 1 and 2 have been taken as collinear. A reasonably good agreement with the experimental results is found for an antiferromagnetic interaction with $J/k_B = -0.02$ K (see Fig. 4). This interaction is likely dominated by intramolecular dipole-dipole interactions, which would give rise to -0.044 K $\leq J/k_B \leq +0.131$ K, depending on the orientation of the main anisotropy axis z . Therefore, Eq. (2) must be regarded as a simplified description, with an effective isotropic J , of the energy level scheme and the overall magnetic moment of [Gd₂].

The results of EPR measurements performed on [Gd₂] are also compatible with the existence of a magnetic interaction between the two Gd ions. Figure 5 shows results measured with X-band and Q-band cavities. These spectra are not simple superpositions

of those measured on the **[LaGd]** and **[GdLu]** monomers (see Figure S3). The strength of J is, however, quite small as compared with that of the single-ion anisotropies. Whereas the latter give rise to zero-field splittings of order 1-1.5 K (Fig. 2) the energy scale of the JS_1S_2 term is about 0.2 K. For this reason, it is not possible to accurately fit J from EPR data. Yet, as Fig. 5 shows, the results are compatible with calculations performed with the same J inferred from magnetic measurements, albeit with an additional broadening that might point to the existence of some ‘ J -strain’ or, as it might be expected from the discussion above, some anisotropy in the coupling between the two Gd spins.

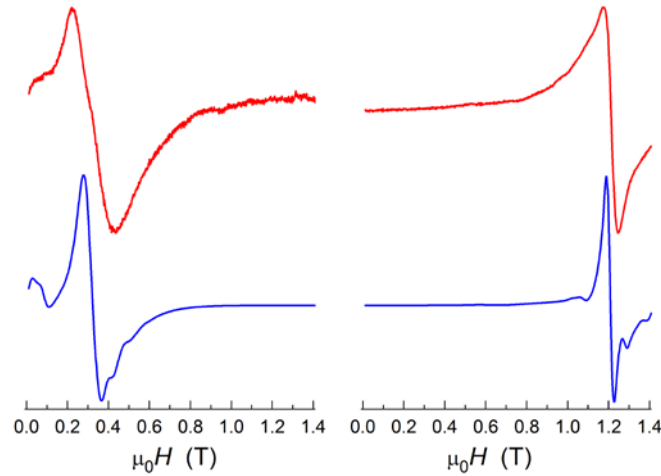


Figure 5. Magnetic spectroscopy of the $[Gd_2]$ dimer. X-band (left) and Q-band (right) cw-EPR spectra measured on a powder sample of $[Gd_2]$ at $T = 6$ K. The curves at the top are experimental results, whereas those at the bottom are results of numerical calculations derived from Eq. (2) with $J/k_B = -0.02$ K.

Similar considerations apply to the results of heat capacity experiments, which are shown in Figure 6. The Schottky anomaly associated with the magnetic anisotropy of both ions dominate data measured above 0.35 K. Still, these data are compatible, within the uncertainties of the experiment and the underlying model, with the predictions derived from Eq. (2) with a $J/k_B = -0.02$ K. For sufficiently strong magnetic fields (see Fig. 6, bottom), the differences between the specific heat data of isolated and coupled spins (and even between those of **[LaGd]** and **[GdLu]**) tend to vanish, as expected.

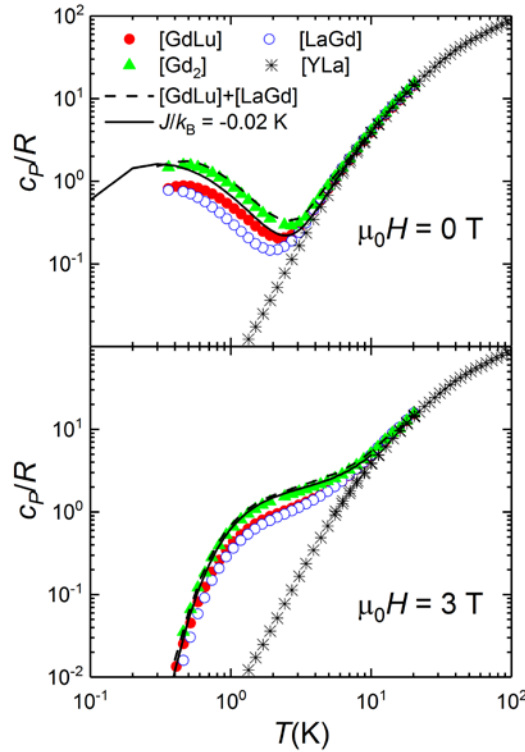


Figure 6. Field-dependent specific heat of the $[\text{Gd}_2]$ dimer. Specific heat of $[\text{Gd}_2]$, compared to those of monomers $[\text{LaGd}]$ and $[\text{GdLu}]$ and of the diamagnetic $[\text{YLa}]$,¹⁹ measured at zero magnetic field (top) and for a strong $\mu_0 H = 3$ T. The dashed line represents the case in which the two spins in $[\text{Gd}_2]$ would not interact. It was obtained by adding the results measured on $[\text{LaGd}]$ and $[\text{GdLu}]$. The solid line shows results of a numerical calculation based on Eq. (2) with $J/k_B = -0.02$ K.

Magnetic energy level scheme: six-qubit encoding and universal operation

The results described in previous sections show that Eq. (2) provides a reasonably good account of the low-lying magnetic energy levels of $[\text{Gd}_2]$. We next discuss, on the basis of this description, the potential of this molecular dimer to implement multiple qubits. The energy scheme of this molecule in a magnetic field, shown in Figure 7, consists of a set of 64 unequally spaced levels, with level separations between adjacent levels of a few GHz. This scheme obviously admits a labelling of the levels in terms of the states of a qudit (from $|n=1\rangle$ for the ground level to $|n=64\rangle$ for the highest excited one) or in terms of the states of six qubits (say, from $|000000\rangle$ to $|111111\rangle$). However, this condition is not sufficient to ensure that such a small “processor” could perform universal quantum operations. The condition of universality implies that *any* quantum superposition of the basis states (the 64 mentioned above) can be generated starting from any initial state, e.g. starting from the system initialized in its ground state. This condition implies that there exist transitions between different levels, which can be univocally addressed by setting the frequency of a microwave pulse or the external magnetic field, and which form a complete set, in the sense, defined above, of allowing “visiting” all possible spin states.

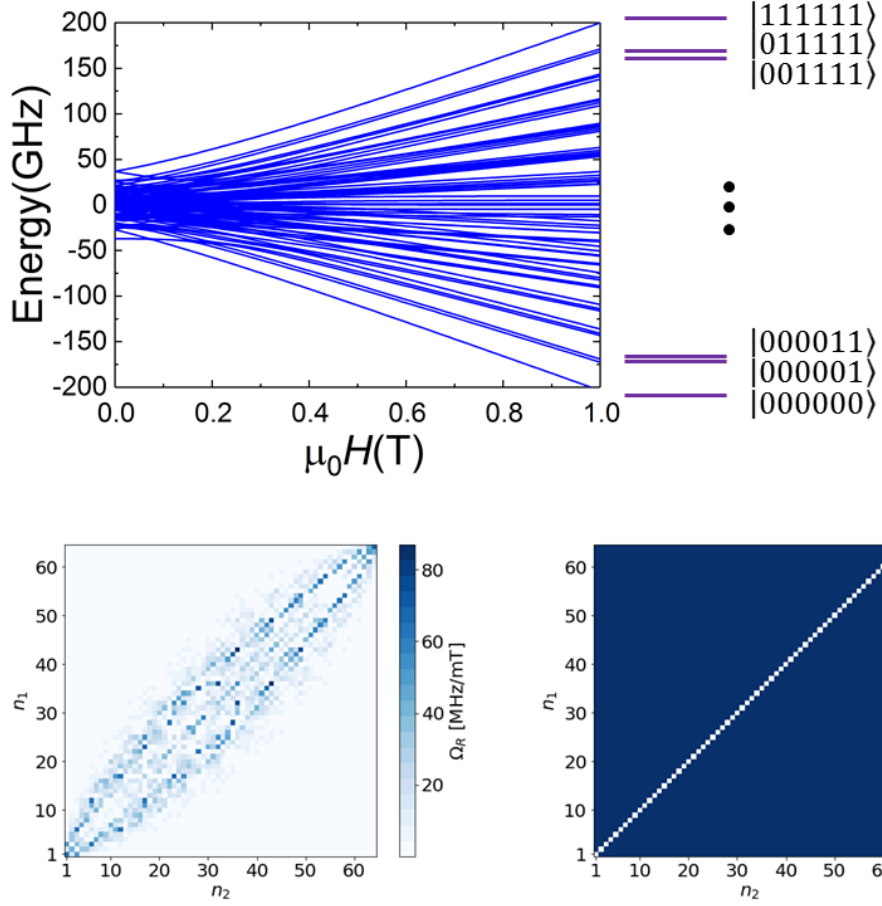


Figure 7. Six-qubit encoding and universality in the $[\text{Gd}_2]$ dimer. Top: Energy level scheme of $[\text{Gd}_2]$ calculated with Eq. (2) and the parameters given in the text. The magnetic field is oriented along the diagonal between the magnetic axes x , y and z of the two $\text{Gd}(\text{III})$ ions, which are taken as collinear for simplicity. A possible labelling of the levels in terms of the basis states of six qubits is shown, in which adjacent levels differ only in the state of one qubit. Bottom, left: Colour map of the Rabi frequencies, calculated at $\mu_0 H = 0.5$ T, linking different levels, numbered from 1, for the ground level, up to 64, for the highest energy one. Bottom, right: map of transitions accessible by concatenating different allowed resonant transitions, showing that the $[\text{Gd}_2]$ system allows universal operations.

The bottom panel of Fig. 7 (left) shows the Rabi frequencies for photon-induced resonant transitions between any two levels. This plot shows a dense map of allowed transitions, with rates exceeding 10-15 MHz/mT, which link the ground state with any other basis state. In order to perform a more rigorous demonstration, we have adapted the mathematical proof for universality,⁴² based on the formalism of Lie algebras, to this particular situation. The bottom right panel of Fig. 7 shows that any two states of the basis can be connected by concatenation of resonant transitions. Using this method, we find also that the Hamiltonian given by Eq. (1) affords a complete set of operations for each qudit (see Fig. S4). However, Eq. (2), which describes the two qudits in $[\text{Gd}_2]$, is universal only when $J \neq 0$ (compare Fig. 7 with Fig. S5, which illustrates the situation for

$J = 0$). The reason for this condition, which we anticipated above, is that conditional operations between states of the two Gd(III) ions can only be implemented with simple resonant pulses if and only if the two are magnetically coupled.

Quantum spin coherence and relaxation

The previous section shows that **[Gd₂]** provides a suitable platform for a six-qubit quantum processor. However, it also sets stringent conditions, namely that transitions between these levels exist and that these transitions can be implemented coherently. The latter depends on the spin-coherence and spin-relaxation times, which we discuss in this section. The spin dynamics has been experimentally studied, at 6 K, on diluted solutions of **[LaGd]**, **[GdLu]** and **[Gd₂]** in MeOH-*d*⁴:EtOH-*d*⁶, with concentrations in the range 0.38-0.61 mmol/L. For all three systems, Electron Spin-Echo (ESE) is observed over the entire 10-810 mT range of magnetic fields used, either using 2- or 3-pulse sequences (Figures S6-S9).

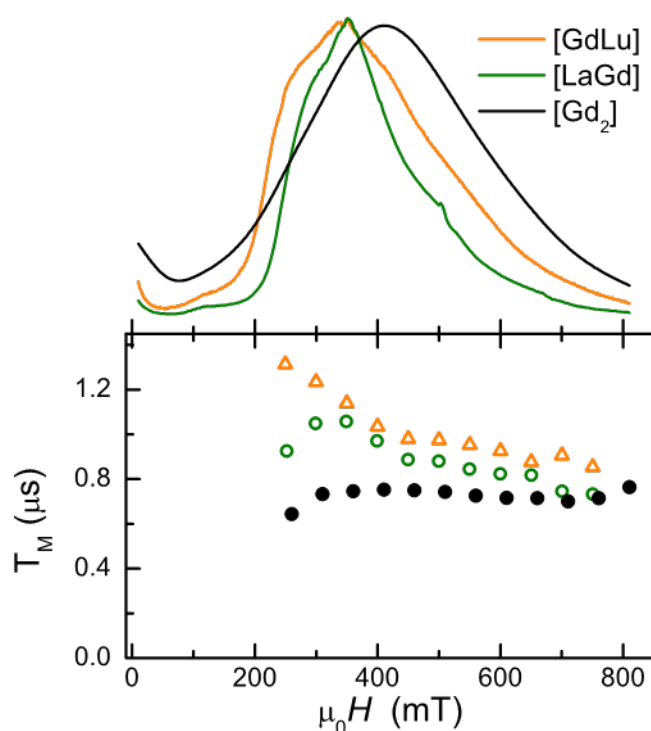


Figure 8. Spin coherence of the molecular qubits. Comparison of the ESE-detected EPR spectra (top) and the field dependence of the phase memory times T_M (bottom), measured on diluted MeOH-*d*⁴:EtOH-*d*⁶ solutions of **[LaGd]**, **[GdLu]** and **[Gd₂]** at 6 K.

Therefore, both the isolated qubits in **[LaGd]** and **[GdLu]** and the exchange-coupled pair in **[Gd₂]** present measurable quantum coherence over the full magnetic field range, thus supporting the picture discussed in the previous section. The echo intensity varies with H , which allows obtaining echo-induced EPR spectra. These are in good agreement with the cw spectra, although the presence of a strong modulation of the echo decay (see below) results in variations with the time interval between pulses (Figs. S7 and S8).

Phase memory times T_M have been obtained by measuring the spin echo decay following a Hahn sequence of $\pi/2$ and π pulses separated by a varying interval τ . For all three compounds, the ESE intensity decreases in a similar manner with increasing τ , the decay being slightly more rapid in the case of **[Gd₂]**. The ESE decay exhibits a strong modulation with a frequency that increases with H , independently of the compound. To quantify these effects, the ESE decays were modelled (Fig. S10) through the equation

$$y(\tau) = y_0 + A_{2p} e^{-2\tau/T_M} \{1 + k e^{-\lambda\tau} \cos(2\pi\nu\tau + \phi)\} \quad (3)$$

in which A_{2p} is the initial amplitude, k the relative amplitude of the modulated signal, λ the additional decay of the oscillating component and ν its frequency, and ϕ the non-zero phase due to the detector dead-time. The magnetic field dependence of A_{2p} exhibits a maximum in the range 300-450 mT, slightly broader for **[GdLu]** than **[GdLa]** (Fig. S12). The **[Gd₂]** data are further broadened and cannot be obtained as a combination of those of **[LaGd]** and **[GdLu]**, in agreement with the cw-EPR results (see Fig. 5, S3 and S9). The phase coherence times of the isolated qubits in **[LaGd]** and **[GdLu]** are similar, although slightly larger for the later (Fig. 8). In both cases, T_M decreases with H , respectively from 1.05/1.31 μ s at 300 mT to 0.73/0.85 μ s at 750 mT. On the contrary, T_M of **[Gd₂]** remains virtually constant at *ca.* 0.73 μ s for all applied fields. Remarkably, the phase memory times derived for the isolated qubits in **[LaGd]** and **[GdLu]** are about twice longer than those found in a 1% magnetically-diluted crystal of the polyoxometallate **[GdW₃₀]**.²⁹ The significantly shorter coherent times found for **[Gd₂]** are in agreement with it being more sensible to decoherence. This can reasonably be associated with the coupling between the two spins, which results in the presence of more possible excitations contributing to decoherence. This suggests that states of the two coupled Gd(III) ions feel decoherence sources affecting either site 1 or site 2. As it happens with other properties (see e.g. Fig. 6), the differences between T_M of the monomers and of **[Gd₂]** are also progressively reduced as the magnetic field increases and the Zeeman interaction dominates over the spin-spin coupling.

Spin-lattice relaxation times T_1 have been determined through the decay of the echo amplitude after a $\pi/2 - \tau - \pi/2 - T - \pi/2$ 3-pulse sequence. In all three compounds, the ESE intensity decreases with increasing interval T , and a similar modulation as that observed in the 2-pulse experiments is present. For this reason, the ESE decay curves were modelled (Fig. S11) with the same equation (3), simply replacing A_{2p} with A_{3p} , 2τ with T and T_M with T_1 . The field-dependences of A_{3p} (Fig. S13) resemble those of A_{2p} , again with broader maxima for **[Gd₂]**, that cannot be obtained as a combination those of **[LaGd]** and **[GdLu]**. Values of T_1 for **[LaGd]** and **[GdLu]** are virtually identical, in the range 2.8-3.2 μ s (Fig. S13) and only slightly lower for the former sample, and independent of H . Only a slight decrease is observed above 550 mT. As for T_M , values of T_1 for the exchange-coupled **[Gd₂]** are significantly lower, *ca.* 2.2 μ s, with a slight increase above 350 mT to reach 2.6 μ s at the highest fields, *i.e.* values close to those of the isolated monomers.

The frequency of the ESE modulation in both the 2- and 3-pulses experiments is very close to twice the Larmor frequency of the ^{15}N nucleus over the whole range of magnetic fields and for the three compounds (Figs. S12 and S13). Clearly, it can be ascribed to the coupling to pyridine N directly coordinated at both sites in the molecular structures. Considering that the flip-flop transition of the electron spin and a quadrupolar nuclear spin is allowed, it is likely that decoherence in these molecules is dominated by the coupling to the $l = 1$ at the coordinated nitrogen atoms.

Coherent control: Rabi oscillations

Spin nutation experiments were performed at 6 K on the same diluted $\text{MeOH-}d^4\text{:EtOH-}d^6$ solutions of **[LaGd]**, **[GdLu]** and **[Gd₂]**. This involves the measurement of the ESE generated by a variable duration pulse ($0.1 \leq t_p \leq 1.6 \mu\text{s}$) refocused by a π pulse, with τ intervals ($100 \leq \tau \leq 200 \text{ ns}$) between the two pulses and between the refocusing pulse and ESE detection. Representative results are shown in Fig. 9 (for **[Gd₂]**) and in the supplementary material (Figs. S14-S16) for **[LaGd]** and **[GdLu]**. In all cases, a strongly damped coherent oscillation is observed. Its frequency depends on the microwave pulse amplitude B_1 , as expected for Rabi oscillations, thus allowing to discriminate them from modulations arising from the coupling to nuclear spins. These additional oscillations become apparent in data measured for longer t_p , once the main Rabi oscillation has decayed. Their frequencies are independent of B_1 but vary linearly with the static magnetic field H . The very fast decay of the main Rabi oscillation and the presence of these additional oscillations hinder a proper modelling of the data, and therefore accurately deriving the damping rate τ_R^{-1} . Nevertheless, a Fourier transformation of the time-dependent oscillations allows an estimation of the mean Rabi frequency. At 410 mT and an attenuation of 10 dB, which corresponds to a microwave field amplitude $B_1 \leq 0.275 \text{ mT}$,²⁹ we find $\Omega_R \approx 12 \text{ MHz}$ for **[LaGd]** and $\Omega_R \approx 17 \text{ MHz}$ for **[GdLu]**. In addition, it reveals two additional frequencies that coincide with twice the Larmor frequency of the ^{15}N nucleus and the Larmor frequency of the ^1H nucleus (Fig. 9 and S14-S16). They result from a cross-polarization of these nuclei by the Gd spin, known as Hartmann-Hahn effect,⁴³ and confirms that the Gd spin is coupled to the surrounding nitrogen and proton nuclear spins, likely contributing to the quantum spin decoherence.

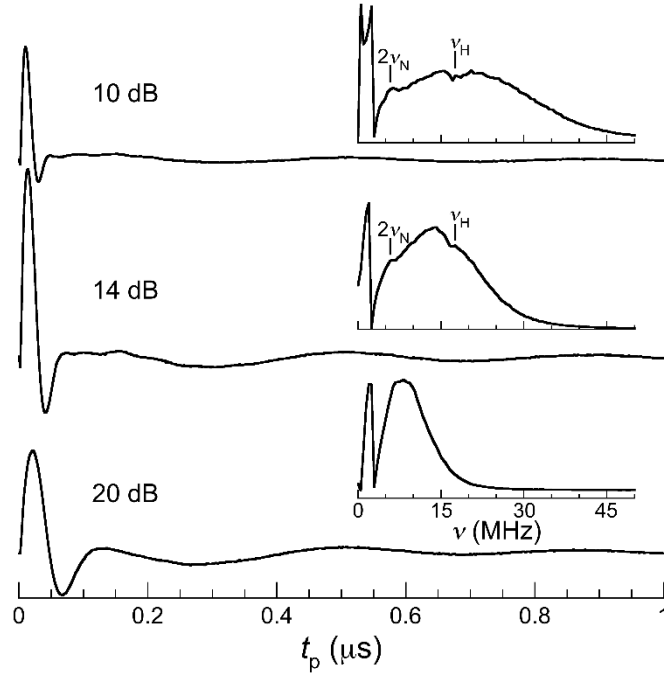


Figure 9. Spin nutation for the $[\text{Gd}_2]$ dimer. Experiments were performed at $T = 6$ K, $\mu_0 H = 410$ mT, that is, close to the maximum observed in the echo-induced spectrum, and for three different microwave pulse powers (attenuations of 10 dB, 14 dB and 20 dB corresponding to $B_1 \approx 0.275$ mT, 0.16 mT and 0.092 mT, respectively), on a diluted $\text{MeOH-}d^4$: $\text{EtOH-}d^6$ solution of $[\text{Gd}_2]$. For each set of data, the Fourier transform is shown as inset, evidencing oscillations with characteristic frequencies that correspond to twice the Larmor frequency of ^{15}N and to the Larmor frequency of ^1H , as indicated, in addition to the main Rabi frequency.

A similar behaviour is observed for $[\text{Gd}_2]$, albeit the Rabi oscillation is then even more strongly damped, decaying completely after the second oscillation (Fig. 9). This faster decay can be at least partially ascribed to the lower T_M of the exchange-coupled Gd(III) spins in $[\text{Gd}_2]$ with respect to the isolated ones in $[\text{LaGd}]$ and $[\text{GdLu}]$. Nevertheless, the nutation observed for the latter is also rather poor. Clearly, working on solutions of randomly oriented molecules imposes strong limitations to these Rabi oscillation studies. Combined with the finite magnetic anisotropy, the random orientation gives rise to many different transitions contributing to the nutation signal, thus to a distribution of Rabi frequencies (see Fig. 7 and Fig. S4). The phase mismatch between the different oscillations shortens severely the time lapse over which nutations can be observed. This effect would be even stronger in the case of $[\text{Gd}_2]$. This explains why the quantum “quality factor” $\Omega_R \tau_R \approx 1$ in these experiments is even smaller than that found for lanthanide qubits in crystalline samples, for which $\Omega_R \tau_R$ are limited only by T_M and by inhomogeneities and fluctuations of the driving microwave field.^{44,45}

In spite of these limitations, the observation of clearly identifiable Rabi oscillations confirms that the relevant transitions in either $[\text{LaGd}]$, $[\text{GdLu}]$ (that realize isolated $d = 8$ qudit operations) and in $[\text{Gd}_2]$ (that implement operations in a $d = 64$ qudit) can be coherently controlled. Besides, the Rabi frequencies observed experimentally lie within

the range of values expected for these systems. Better stability of the Rabi oscillations and therefore $\Omega_R \tau_R$ can be expected for diluted solids as well as for isolated molecules integrated into hybrid devices.

Discussion

In this work, we have designed a molecular structure that can host two Gd(III) ions in distinct coordination environments. Combined with the intrinsic properties of this ion, in particular its $S = 7/2$ and zero orbital moment, this design enables realizing two different spin qudits, each with $d = 8$ or, equivalently, three qubits. These qudits can be studied in isolation, in either **[LaGd]** and **[GdLu]** molecules in which they are accompanied by a diamagnetic counterpart, or can be both integrated in the same molecular unit. In the latter case, we have shown that the molecular dimer **[Gd₂]** meets all conditions needed to realize six qubits (or a $d = 64$ qudit).

The integration of a high number of addressable quantum states in well-defined molecular units represents one of the distinctive traits of the chemical approach to quantum technologies, and can provide a number of competitive advantages in this field. Such molecules can locally act as tiny quantum processors themselves, the equivalent of NISQS (Noisy Intermediate Size Quantum Systems) in other schemes,⁴⁶ thus implementing simple algorithms. Of special relevance would be the correction of errors, e.g. phase errors that are likely to be most disturbing in the case of spin qubits, at the molecular scale.^{27,30} For this, it is not even necessary that the dimension of the Hilbert space defined by the available spin states be a power of two. These molecular NISQS can also serve as a suitable basis where to map quantum simulations of simple systems, such as small molecules.^{33,47} An advantage of using a single physical unit to perform these simple computations is that it reduces the number of non-local operations, which require switching on and off interactions between different parts of a quantum circuit, and that are often more sensitive to decoherence and, therefore, error.^{31,32}

The fulfilment of this potential defines also a series of important challenges. The first is to get rid of the limitations associated with the need of reducing dipolar decoherence, which often require working on randomly oriented ensembles of molecules in solution. This difficulty can be overcome by either creating well-organized molecular frameworks, in which all molecules need to be oriented in the same manner and, at the same time, magnetically diluted or sufficiently far away from each other.⁴⁸⁻⁵⁰ In the end, the ideal situation would be to explore the response of individual molecules, either via the application of single-molecule electronics^{24,25,28} or by enhancing the current sensitivity of magnetic spectroscopic techniques.⁵¹⁻⁵³

A second challenge is how to move forward beyond the level of a few qubits. As it becomes clear by inspecting the energy level scheme of a $d = 64$ qudit, the resonant transitions that provide the basic set of operations suffers already from a “frequency crowding”. Therefore, scaling beyond this point must proceed by linking different units via coherent mediators. Implementing such switchable couplings within molecules (e.g.

via chemical linkers sensitive to some external stimuli, such as light) remains a challenging goal.^{22,54,55} The alternative is to combine a chemical, bottom up, approach with the integration of functional molecules into solid-state devices. A recent proposal for a scalable architecture considers the possibility of applying superconducting circuits, namely on-chip resonators, to control, read-out and communicate magnetic molecules.^{56,57} Within this scheme, medium size molecular qudits, able to embed some critical functionalities such as phase error correction, would provide very attractive building blocks to reach computational performances difficult to match by other platforms.

Methods

Synthesis

6-(3-oxo-3-(2-hydroxyphenyl)propionyl)pyridine-2-carboxylic acid (H₃L). The ligand H₃L was synthesized as described previously.¹⁴

(Hpy)[Gd₂(HL)₃(NO₃)(py)(H₂O)]·5py ([Gd₂]). Compound [Gd₂] was synthesized as described previously.¹⁵ Purity was checked by elemental analysis, mass spectrometry and multiple cell determinations on single crystals, including full structure determination.

(Hpy)[LaGd(HL)₃(NO₃)(py)(H₂O)]·5py ([LaGd]). A 10 mL pyridine solution of ligand H₃L (30.0 mg, 0.105 mmol) is added slowly to a 10 mL pyridine solution of La(NO₃)₃·6H₂O (15.2 mg, 0.035 mmol) and Gd(NO₃)₃·6H₂O (15.8 mg, 0.035 mmol). The mixture is stirred at room temperature for one hour, yielding a clear shiny yellow solution that is layered with diethylether. Crystals of [LaGd] form slowly and are recovered after one week in a 63 % yield. ESI-MS: [LaGd(HL)₂(H₂L)]⁺ m/z = 1146.98. Elemental analysis found (calc.) for [LaGd(H₂L)(HL)₂(NO₃)(py)(H₂O)]·3H₂O: C 44.11 (44.16); H 2.77 (3.04); N 4.87 (5.15). IR (KBr, ν/cm^{-1}): 3410m, 1618s, 1583s, 1560m, 1528s, 1463m, 1400s, 1384s, 1298m, 1239w, 1204w, 1148w, 1120w, 1059m, 949m, 891w, 760m, 706m, 663m, 635w, 568w.

(Hpy)[GdLu(HL)₃(NO₃)(py)(H₂O)]·5py ([GdLu]). A 10 mL pyridine solution of ligand H₃L (30.0 mg, 0.105 mmol) is added slowly to a 10 mL pyridine solution of Gd(NO₃)₃·6H₂O (15.8 mg, 0.035 mmol) and Lu(NO₃)₃·6H₂O (16.4 mg, 0.035 mmol). The mixture is stirred at room temperature for one hour, yielding a clear yellow solution to which 200 mL conc. HNO₃ is added. After 10 more min stirring, the solution is layered with diethylether. Crystals of [GdLu] are recovered after 2 weeks in a 53% yield. ESI-MS: [GdLu(HL)₂(H₂L)]⁺ m/z = 1183.02. Elemental analysis found (calc.) for [GdLu(H₂L)(HL)₂(NO₃)(py)(H₂O)]·3H₂O: C 40.22 (43.01); H 2.47 (2.96); N 5.21 (5.02). IR (KBr, ν/cm^{-1}): 3422m, 1619s, 1585s, 1560m, 1528s, 1465m, 1401s, 1384s, 1325m, 1299m, 1239w, 1208w, 1147w, 1121w, 1058m, 950m, 892w, 756w, 708m, 666w, 637w, 569w.

Magnetic measurements

Magnetic measurements were performed using a Quantum Design SQUID MPMS-XL magnetometer through the Physical Measurements unit of the Servicio de Apoyo a la

Investigación-SAI, Universidad de Zaragoza. All data were corrected for the sample holders and grease contributions, determined empirically as well as for the intrinsic diamagnetism of the sample, estimated using Pascal constants.

Heat capacity experiments

Heat capacity data were measured, down to $T = 0.35$ K, with a commercial physical property measurement system (PPMS, Physical Measurements unit of the Servicio de Apoyo a la Investigación-SAI, Universidad de Zaragoza) that makes use of the relaxation method. The samples, in powder form, were pressed into pellets and placed onto the calorimeter on top of a thin layer of Apiezon N grease that fixes the sample and improves the thermal contact. The raw data were corrected from the known contributions arising from the empty calorimeter and the grease.

Electron Paramagnetic Resonance experiments

Continuous wave (cw) EPR measurements were performed with a Bruker Biospin ELEXSYS E-580 spectrometer operating in the X-band and Q-band. In addition, pulsed Time Domain (TD) measurements were performed at X-band frequencies. Solid-state cw-EPR measurements were performed at RT on polycrystalline samples in quartz tubes. TD-EPR measurements were done on frozen solutions, for which gas-flow Helium cryostats were used. The polycrystalline solids were dissolved in a 1:1 mixture of fully-deuterated methanol and ethanol. The use of deuterated solvents is intended to limit decoherence due to protons. The TD-EPR experiments were performed at 6 K on 0.61 ([LaGd]), 0.38 ([GdLu]) and 0.44 ([Gd₂]) mmol/L solutions. Measurements on 0.13 and 0.08 mmol/L solutions of [GdLu] were also performed to discard any variation of T_1 and T_M in the range of concentrations used. For comparison, cw-EPR measurements were also done on the same frozen solutions, albeit in the range 20-80 K due to signs of saturation at 6 K.

Single Crystal X-ray Diffraction

Data for compounds [LaGd] and [GdLu] were collected at 100 K on a Bruker APEX II QUAZAR diffractometer equipped with a microfocus multilayer monochromator with MoK α radiation ($\lambda = 0.71073$ Å), respectively on a yellow lath and a yellow needle of dimensions 0.86x0.18x0.12 and 0.40x0.03x0.03 mm³. Data reduction and absorption corrections were performed with SAINT and SADABS,⁵⁸ respectively. Both structures were solved by intrinsic phasing with SHELXT⁵⁹ and refined by full-matrix least-squares on F^2 with SHELXL-2014.⁶⁰ In the case of [GdLu], remaining voids in the structure with no significant electron density peaks were analysed and taken into account with PLATON SQUEEZE⁶¹ that recovered a total of 224 electrons per cell, over four equivalent voids of 193 Å³. These figures being reasonable for one diffuse pyridine solvent molecule per void, *i.e.* one per formula unit, this has been reflected in the reported formula. For both structures, the metal site composition was confirmed by refining the structure with the two homometallic situations as well as with the Ln sites inverted. These resulted in relatively poorer agreement factors and most importantly in unrealistic combinations of U_{eq} values at the metal sites.

Theory: universality test for molecular spin qudits

A universal quantum processor must be able to implement any unitary operation within the computational states embedded in a Hilbert space. In the particular case discussed here, i.e. qudits simulating qubits: any transition between two molecular states must be driven by applying an external field. To show if a particular molecular qudit is universal (in this sense) or not, we write the spin Hamiltonian as,

$$\mathcal{H} = \mathcal{H}_s - g\mu_B \vec{H}_{ext}(t) \vec{S} \quad (4)$$

Here, \vec{S} is the total spin operator and $\vec{H}_{ext}(t)$ is a time-dependent external magnetic field that induces resonant transitions between different eigenstates of the spin Hamiltonian \mathcal{H}_s . These eigenstates form the computational basis. Since the dimension d of the Hilbert spaces of all spin qudits considered in this work is $d = 2^N$, with $N = 3$ for **[LaGd]** and **[GdLu]**, and $N = 6$ for **[Gd₂]**, these eigenstates may be denoted as either $|n\rangle$ (with $n = 1, \dots, d$) or as $|0\ 0 \dots 0\rangle$ to $|1\ 1 \dots 1\rangle$. If all of these states are accessible from any other one, the qudit realizes a N -qubit processor.

One way to check universality is as follows. We use the fact that the energy spectrum has some nonlinearity, i.e. that the levels are not simply equidistant as those of a harmonic oscillator. This arises from the combination of single ion anisotropy, the dissymmetry between the two Gd(III) coordination sites and the mutual interaction between the two Gd(III) spins. This means that we can address a transition between any two states, say $|n\rangle$ and $|m\rangle$, by making the frequency ω of the driving magnetic field $\vec{H}_{ext}(t)$ resonant with the transition frequency $\omega_{nm} = (E_n - E_m)/\hbar$, provided that the matrix element $\langle n | \vec{H}_{ext}(t) \cdot \vec{S} | m \rangle \neq 0$. If this happens, it is fair to say that we can implement any unitary operation of the form $e^{iH_{nm}t}$ with $H_{nm} = |n\rangle\langle m| + h.c.$ The allowed transitions define a set $L = \{H_{nm}, H_{n'm'}, \dots\}$

It is however expected that L will not cover *all* the necessary transitions. The natural question is then which extra transitions can be implemented by concatenating the different elements of L . The formal answer⁶² to this question is that the accessible transitions are those belonging to the Lie algebra \mathcal{L} generated by L . This is a natural consequence of the Lie-Trotter formulas, i.e.

$$e^{i[H_{nm}, H_{n'm'}]t} = \lim_{C \rightarrow \infty} \left(e^{\frac{H_{nm}t}{\sqrt{C}}} e^{\frac{H_{n'm'}t}{\sqrt{C}}} e^{-\frac{H_{nm}t}{\sqrt{C}}} e^{-\frac{H_{n'm'}t}{\sqrt{C}}} \right)^C \quad (5)$$

The different commutators of the elements of L are also elements of the corresponding Lie group, \mathcal{L} . In practice, to find the allowed transitions, we may compute the H_{nm} by expressing $g\mu_B \vec{H}_{ext}(t) \vec{S}$ in the basis of eigenstates of \mathcal{H}_s and compute all possible commutators. By doing so, we can check if \mathcal{L} covers the full Hilbert space. In a finite dimensional basis, this is easily computed since the non-zero commutators are of the form:

$$i [H_{nm}, H_{n'm'}] = i |m\rangle\langle m'| + h.c. \quad (6)$$

We finally notice that the proof says nothing about how to perform operations. It only checks if they are possible.

Universality of [GdLu] and [LaGd] three-qubit systems (or qu8its). These molecules have a spin Hamiltonian \mathcal{H}_S given by Eq. (1). It is rather simple to prove that this Hamiltonian leads to universal operations. It turns out that for intermediate magnetic fields, say $\mu_0 H_z \sim 0.5 - 1$ T, the level spectrum consists of non-equidistant levels and that $\langle n | S_x | n + 1 \rangle \neq 0$ for all eigenstates $|n\rangle$ (see Fig. S4). From the point of view of universal operation, this is rather favourable since $i [H_{n, n+1}, H_{n+1, n+2}] = i |n\rangle\langle n + 2| + h.c.$, and so on. Therefore, every transition can be performed by concatenating commutators.

Universality of the [Gd₂] six-qubit system (or qu64it). Putting together several qudits, they must interact as a prerequisite to be universal. The [Gd₂] dimer is described by Eq. (2), which includes a weak, antiferromagnetic interaction, thus it fulfils this condition. Besides, from the previous discussion it follows that if some symmetry is shared by \mathcal{H}_S and $\vec{H}_{ext}(t)\vec{S}$, the system is presumably not universal. For example, a parity selection rule can impose that only transitions $\langle n | \vec{H}_{ext}(t)\vec{S} | n + 2 \rangle \neq 0$. Then, this system becomes not universal: starting from an even labeled state $|n\rangle$, the odd states cannot be accessed, and viceversa. This condition might introduce difficulties in situations that are closer to that described by the spin Hamiltonian of [Gd₂]. The isotropic Heisenberg model, $H = -J \vec{S}_1 \vec{S}_2 - g\mu_B \vec{H} (\vec{S}_1 + \vec{S}_2)$ conserves the total spin S . Therefore, a spin dimer described by this model is definitely not universal for an external driving $g\mu_B \vec{H}_{ext} \vec{S}$, with $\vec{S} = \vec{S}_1 + \vec{S}_2$. Transitions between different total spin states are forbidden. Fortunately, in [Gd₂] the different anisotropy terms acting on each spin break this symmetry, besides providing a non-equidistant level spectrum. However, contrary to what happens in the single qudit case, the dc magnetic field H cannot be much higher than J , D and E . The reason is twofold. If H is strong enough, the two Gd(III) ions are effectively decoupled. At the same time, the anisotropy terms become less important and the system is closer to an isotropic Heisenberg system. Our numerical calculations, whose results are shown in Fig. 7 and in Fig. S5, confirm this. The bottom panel (left) of Fig. 7 and the top panels of Fig. S5 show maps of the Rabi frequencies for resonant transitions between any pair of states. Using transitions with Rabi frequencies larger than 0.2 MHz/mT, we construct contour plots (Fig. 7, bottom right panel and bottom panels of Fig. S5) of those transitions that are feasible by concatenation of all possible commutation operators. The system is universal if the matrix built in this way spans all points (except the diagonal). Figure 7 shows the universal character of the dimer of two coupled Gd(III) ions in a not too strong magnetic dc-field. Then, Fig. S5 shows how this property is broken down by either setting $J = 0$ or increasing the dc-external field. The conclusion is that [Gd₂] can, under the appropriate conditions, simulate either a six-qubit processor or two decoupled three-qubit systems.

References

- 1 Awschalom, D. D., Bassett, L. C., Dzurak, A. S., Hu, E. L. & Petta, J. R. Quantum Spintronics: Engineering and Manipulating Atom-Like Spins in Semiconductors. *Science* **339**, 1174-1179, doi:10.1126/science.1231364 (2013).
- 2 Jelezko, F., Gaebel, T., Popa, I., Gruber, A. & Wrachtrup, J. Observation of coherent oscillations in a single electron spin. *Phys. Rev. Lett.* **92**, 4, doi:10.1103/PhysRevLett.92.076401 (2004).
- 3 Pla, J. J. *et al.* A single-atom electron spin qubit in silicon. *Nature* **489**, 541-545, doi:10.1038/nature11449 (2012).
- 4 Gaita-Ariño, A., Luis, F., Hill, S. & Coronado, E. Molecular spins for quantum computation. *Nature Chem.* **11**, 301-309, doi:10.1038/s41557-019-0232-y (2019).
- 5 Atzori, M. & Sessoli, R. The Second Quantum Revolution: Role and Challenges of Molecular Chemistry. *J. Am. Chem. Soc.* **141**, 11339-11352, doi:10.1021/jacs.9b00984 (2019).
- 6 Aromí, G., Aguilà, D., Gamez, P., Luis, F. & Roubeau, O. Design of magnetic coordination complexes for quantum computing. *Chem. Soc. Rev.* **41**, 537-546, doi:10.1039/c1cs15115k (2012).
- 7 Martinez-Perez, M. J. *et al.* Gd-Based Single-Ion Magnets with Tunable Magnetic Anisotropy: Molecular Design of Spin Qubits. *Phys. Rev. Lett.* **108**, 247213, doi:10.1103/PhysRevLett.108.247213 (2012).
- 8 Shiddiq, M. *et al.* Enhancing coherence in molecular spin qubits via atomic clock transitions. *Nature* **531**, 348+, doi:10.1038/nature16984 (2016).
- 9 Ardavan, A. *et al.* Will spin-relaxation times in molecular magnets permit quantum information processing? *Phys. Rev. Lett.* **98**, 057201, doi:10.1103/PhysRevLett.98.057201 (2007).
- 10 Bader, K. *et al.* Room temperature quantum coherence in a potential molecular qubit. *Nature Commun.* **5**, 5304, doi:10.1038/ncomms6304 (2014).
- 11 Zadrozny, J. M., Niklas, J., Poluektov, O. G. & Freedman, D. E. Millisecond Coherence Time in a Tunable Molecular Electronic Spin Qubit. *ACS Cent. Sci.* **1**, 488-492, doi:10.1021/acscentsci.5b00338 (2015).
- 12 Atzori, M. *et al.* Room-Temperature Quantum Coherence and Rabi Oscillations in Vanadyl Phthalocyanine: Toward Multifunctional Molecular Spin Qubits. *J. Am. Chem. Soc.* **138**, 2154-2157, doi:10.1021/jacs.5b13408 (2016).
- 13 Atzori, M. *et al.* Quantum Coherence Times Enhancement in Vanadium(IV)-based Potential Molecular Qubits: the Key Role of the Vanadyl Moiety. *J. Am. Chem. Soc.* **138**, 11234-11244, doi:10.1021/jacs.6b05574 (2016).
- 14 Aguila, D. *et al.* Synthesis and Properties of a Family of Unsymmetric Dinuclear Complexes of Ln(III) (Ln = Eu, Gd, Tb). *Inorg. Chem.* **49**, 6784-6786, doi:10.1021/ic1008285 (2010).
- 15 Aguilà, D. *et al.* Lanthanide Contraction within a Series of Asymmetric Dinuclear Ln(2) Complexes. *Chem., Eur. J.* **19**, 5881-5891, doi:10.1002/chem.201204451 (2013).
- 16 Gonzalez-Fabra, J. *et al.* Thermodynamic Stability of Heterodimetallic LnLn Complexes: Synthesis and DFT Studies. *Chem., Eur. J.* **23**, 5117-5125, doi:10.1002/chem.201700095 (2017).

- 17 Aguilà, D. *et al.* Selective Lanthanide Distribution within a Comprehensive Series of Heterometallic LnPr Complexes. *Inorg. Chem.* **57**, 8429-8439, doi:10.1021/acs.inorgchem.8b01112 (2018).
- 18 Luis, F. *et al.* Molecular Prototypes for Spin-Based CNOT and SWAP Quantum Gates. *Phys. Rev. Lett.* **107**, 117203, doi:10.1103/PhysRevLett.107.117203 (2011).
- 19 Aguilà, D. *et al.* Heterodimetallic [LnLn'] Lanthanide Complexes: Toward a Chemical Design of Two-Qubit Molecular Spin Quantum Gates. *J. Am. Chem. Soc.* **136**, 14215-14222, doi:10.1021/ja507809w (2014).
- 20 Aromí, G., Luis, F. & Roubeau, O. in *Lanthanides and Actinides in Molecular Magnetism Wiley Online Books* (eds R. A. Layfield & M. Murugesu) 185-221 (Wiley-WCH, 2015).
- 21 Aromí, G. & Roubeau, O. in *Handbook on the Physics and Chemistry of Rare Earths* Vol. 56 (eds Jean-Claude G. Bünzli & Vitalij K. Pecharsky) 1-54 (Elsevier, 2019).
- 22 Ferrando-Soria, J. *et al.* A modular design of molecular qubits to implement universal quantum gates. *Nature Commun.* **7**, 11377, doi:10.1038/ncomms11377 (2016).
- 23 Ardavan, A. *et al.* Engineering coherent interactions in molecular nanomagnet dimers. *Npj Quantum Information* **1**, 7, doi:10.1038/npjqi.2015.12 (2015).
- 24 Vincent, R., Klyatskaya, S., Ruben, M., Wernsdorfer, W. & Balestro, F. Electronic read-out of a single nuclear spin using a molecular spin transistor. *Nature* **488**, 357, doi:10.1038/nature11341 (2012).
- 25 Moreno-Pineda, E., Godfrin, C., Balestro, F., Wernsdorfer, W. & Ruben, M. Molecular spin qudits for quantum algorithms. *Chem. Soc. Rev.* **47**, 501-513, doi:10.1039/C5CS00933B (2018).
- 26 Moreno-Pineda, E., Damjanović, M., Fuhr, O., Wernsdorfer, W. & Ruben, M. Nuclear Spin Isomers: Engineering a Et₄N[DyPc₂] Spin Qudit. *Angew. Chem., Int. Ed.* **56**, 9915-9919, doi:10.1002/anie.201706181 (2017).
- 27 Hussain, R. *et al.* Coherent Manipulation of a Molecular Ln-Based Nuclear Qudit Coupled to an Electron Qubit. *J. Am. Chem. Soc.* **140**, 9814-9818, doi:10.1021/jacs.8b05934 (2018).
- 28 Godfrin, C. *et al.* Operating Quantum States in Single Magnetic Molecules: Implementation of Grover's Quantum Algorithm. *Phys. Rev. Lett.* **119**, 187702, doi:10.1103/PhysRevLett.119.187702 (2017).
- 29 Jenkins, M. D. *et al.* Coherent manipulation of three-qubit states in a molecular single-ion magnet. *Phys. Rev. B* **95**, 8, doi:10.1103/PhysRevB.95.064423 (2017).
- 30 Pirandola, S., Mancini, S., Braunstein, S. L. & Vitali, D. Minimal qudit code for a qubit in the phase-damping channel. *Phys. Rev. A* **77**, 032309, doi:10.1103/PhysRevA.77.032309 (2008).
- 31 Lanyon, B. P. *et al.* Simplifying quantum logic using higher-dimensional Hilbert spaces. *Nat. Phys.* **5**, 134-140, doi:10.1038/nphys1150 (2009).
- 32 Kiktenko, E. O., Fedorov, A. K., Strakhov, A. A. & Man'ko, V. I. Single qudit realization of the Deutsch algorithm using superconducting many-level quantum circuits. *Phys. Lett. A* **379**, 1409-1413, doi:10.1016/j.physleta.2015.03.023 (2015).
- 33 Kandala, A. *et al.* Hardware-efficient variational quantum eigensolver for small molecules and quantum magnets. *Nature* **549**, 242-246, doi:10.1038/nature23879 (2017).

- 34 D'Angelo, P. *et al.* Revised Ionic Radii of Lanthanoid(III) Ions in Aqueous Solution. *Inorg. Chem.* **50**, 4572-4579, doi:10.1021/ic200260r (2011).
- 35 Ruiz-Martinez, A. & Alvarez, S. Stereochemistry of Compounds with Coordination Number Ten. *Chem., Eur. J.* **15**, 7470-7480, doi:10.1002/chem.200900547 (2009).
- 36 Ruiz-Martinez, A., Casanova, D. & Alvarez, S. Polyhedral structures with an odd number of vertices: Nine-coordinate metal compounds. *Chem., Eur. J.* **14**, 1291-1303, doi:10.1002/chem.200701137 (2008).
- 37 Rinehart, J. D. & Long, J. R. Exploiting single-ion anisotropy in the design of f-element single-molecule magnets. *Chem. Sci.* **2**, 2078-2085, doi:10.1039/c1sc00513h (2011).
- 38 Goodwin, C. A. P., Ortu, F., Reta, D., Chilton, N. F. & Mills, D. P. Molecular magnetic hysteresis at 60 kelvin in dysprosocenium. *Nature* **548**, 439, doi:10.1038/nature23447 (2017).
- 39 Guo, F.-S. *et al.* Magnetic hysteresis up to 80 kelvin in a dysprosium metallocene single-molecule magnet. *Science* **362**, 1400-1403, doi:10.1126/science.aav0652 (2018).
- 40 Stoll, S. & Schweiger, A. EasySpin, a comprehensive software package for spectral simulation and analysis in EPR. *J. Magn. Reson.* **178**, 42-55, doi:10.1016/j.jmr.2005.08.013 (2006).
- 41 Evangelisti, M., Luis, F., de Jongh, L. J. & Affronte, M. Magnetotherma properties of molecule-based materials. *J. Mater. Chem.* **16**, 2534-2549, doi:10.1039/b603738k (2006).
- 42 Kraus, C. V., Wolf, M. M. & Cirac, J. I. Quantum simulations under translational symmetry. *Phys. Rev. A* **75**, 9, doi:10.1103/PhysRevA.75.022303 (2007).
- 43 Hartmann, S. R. & Hahn, E. L. NUCLEAR DOUBLE RESONANCE IN ROTATING FRAME. *Physical Review* **128**, 2042-&, doi:10.1103/PhysRev.128.2042 (1962).
- 44 Bertaina, S. *et al.* Rare-earth solid-state qubits. *Nat. Nanotechnol.* **2**, 39, doi:10.1038/nnano.2006.174 (2007).
- 45 Bertaina, S., Shim, J. H., Gambarelli, S., Malkin, B. Z. & Barbara, B. Spin-Orbit Qubits of Rare-Earth-Metal Ions in Axially Symmetric Crystal Fields. *Phys. Rev. Lett.* **103**, 4, doi:10.1103/PhysRevLett.103.226402 (2009).
- 46 Preskill, J. Quantum Computing in the NISQ era and beyond. *Quantum* **2**, 20 (2018).
- 47 Chiesa, A. T., F. Grossi, M. Santini, P. Tavernelli, I. Gerace, D. Carreta, S. Quantum hardware simulating four-dimensional inelastic neutron scattering. *Nature Phys.* **15**, 455-459 (2019).
- 48 Zadrozny, J. M., Gallagher, A. T., Harris, T. D. & Freedman, D. E. A Porous Array of Clock Qubits. *J. Am. Chem. Soc.* **139**, 7089-7094, doi:10.1021/jacs.7b03123 (2017).
- 49 Urtizbera, A. *et al.* A Porphyrin Spin Qubit and Its 2D Framework Nanosheets. *Adv. Funct. Mater.* **28**, 1801695, doi:10.1002/adfm.201801695 (2018).
- 50 Urtizbera, A. *et al.* Vanadyl spin qubit 2D arrays and their integration on superconducting resonators. *Materials Horizons* **7**, 885-897, doi:10.1039/C9MH01594A (2020).
- 51 Jenkins, M. D. *et al.* Nanoscale constrictions in superconducting coplanar waveguide resonators. *Appl. Phys. Lett.* **105**, 5, doi:10.1063/1.4899141 (2014).
- 52 Bienfait, A. *et al.* Reaching the quantum limit of sensitivity in electron spin resonance. *Nat. Nanotechnol.* **11**, 253-257, doi:10.1038/nnano.2015.282 (2016).

- 53 Eichler, C., Sigillito, A. J., Lyon, S. A. & Petta, J. R. Electron Spin Resonance at the Level of 10(4) Spins Using Low Impedance Superconducting Resonators. *Phys. Rev. Lett.* **118**, 5, doi:10.1103/PhysRevLett.118.037701 (2017).
- 54 Lehmann, J., Gaita-Arino, A., Coronado, E. & Loss, D. Spin qubits with electrically gated polyoxometalate molecules. *Nat. Nanotechnol.* **2**, 312-317, doi:10.1038/nnano.2007.110 (2007).
- 55 Salinas-Uber, J. *et al.* Molecules Designed to Contain Two Weakly Coupled Spins with a Photoswitchable Spacer. *Chem., Eur. J.* **23**, 13648-13659, doi:10.1002/chem.201702171 (2017).
- 56 Jenkins, M. *et al.* Coupling single-molecule magnets to quantum circuits. *New Journal of Physics* **15**, 22, doi:10.1088/1367-2630/15/9/095007 (2013).
- 57 Jenkins, M. D. *et al.* A scalable architecture for quantum computation with molecular nanomagnets. *Dalton Trans.* **45**, 16682-16693, doi:10.1039/c6dt02664h (2016).
- 58 SAINT and SADABS (Bruker AXS Inc., Madison, Wisconsin, USA, 2012).
- 59 Sheldrick, G. SHELXT - Integrated space-group and crystal-structure determination. *Acta Cryst. A* **71**, 3-8, doi:doi:10.1107/S2053273314026370 (2015).
- 60 Sheldrick, G. Crystal structure refinement with SHELXL. *Acta Cryst. C* **71**, 3-8, doi:doi:10.1107/S2053229614024218 (2015).
- 61 Spek, A. PLATON SQUEEZE: a tool for the calculation of the disordered solvent contribution to the calculated structure factors. *Acta Cryst. C* **71**, 9-18, doi:doi:10.1107/S2053229614024929 (2015).
- 62 Kraus, C. V., Wolf, M. M. & Cirac, J. I. Quantum simulations under translational symmetry. *Phys. Rev. A* **75**, 022303, doi:10.1103/PhysRevA.75.022303 (2007).

Acknowledgements

This work was supported by funds from the EU (ERC Starting Grant 258060 FuncMolQIP, COST Action 15128 MOLSPIN, QUANTERA project SUMO, FET-OPEN grant 862893 FATMOLS), the Spanish MICINN (grants CTQ2015-68370-P, CTQ2015-64486-R, RTI2018-096075-B-C21, PCI2018-093116, PGC2018-098630-B-I00, MAT2017-86826-R) and the Gobierno de Aragón (grants E09-17R-Q-MAD, E31_17R PLATON). GA thanks the Generalitat de Catalunya for the prize ICREA Academia 2018.

Authors' contributions

V. V., D. A., L. A. B. and G. A. designed and synthesized the molecular complexes. O. R. performed the heat capacity measurements, O. R. and F. L. performed the magnetic measurements and P. J. A. and O. R. performed the EPR measurements. F. L. modelled the heat capacity and magnetic data and P. J. A. modelled the EPR results. D. Z. performed the quantum universality analysis. G. A. and F. L. conceived the idea and supervised the project. G. A., O. R. and F. L. wrote the paper with input from all co-authors.

Accession codes

All details can be found in CCDC 1999444 (**[LaGd]**) and 1999445 (**[GdLu]**) that contain the supplementary crystallographic data for this paper. The structure of **[Gd₂]** has been reported previously and can be found in CCDC 915331. These data can be obtained free of charge from The Cambridge Crystallographic Data Centre via <https://summary.ccdc.cam.ac.uk/structure-summary-form>. Crystallographic and refinement parameters for **[LaGd]** and **[GdLu]** are summarized in Table S1. Selected bond lengths and angles and hydrogen bonds details are given in Tables S2 and S3 respectively.

Competing financial interests

The authors state they have no competing financial interests.

A dissymmetric [Gd₂] coordination molecular dimer hosting six addressable spin qubits

Fernando Luis, Pablo J. Alonso, Olivier Roubeau, Verónica Velasco, David Zueco, David Aguilà, Leoní A. Barrios, Guillem Aromí

Table of contents

Table S1. Crystallographic and refinement parameters of [LaGd] and [GdLu]	p. S2
Table S2. Coordination environment of the Gd sites in [LaGd] and [GdLu]	p. S3
Table S3. Details of H-bonding in [LaGd] and [GdLu]	p. S4
Figure S1. H-bonding in the structures of [LaGd] and [GdLu]	p. S5
Figure S2. Continuous shape measures for the Gd sites in [LaGd] and [GdLu]	p. S6
Figure S3. CW-EPR spectra at X and Q bands for [LaGd] , [GdLu] and [Gd₂]	p. S7
Figure S4. Calculated transition and Rabi frequencies for resonant transitions in [LaGd]	p. S8
Figure S5. Universality test for [Gd₂]	p. S9
Figure S6. Representative spin-echo decay for [LaGd] , [GdLu] and [Gd₂]	p. S10
Figure S7. Echo-induced EPR spectra from 2-pulse experiments and varying τ .	p. S11
Figure S8. Echo-induced EPR spectra from 3-pulse experiments and varying T.	p. S12
Figure S9. Echo-induced EPR spectra from sums over τ and T.	p. S13
Figure S10 A, B and C. Modelization of 2-pulse electron spin-echo decays	p. S14
Figure S11 A, B and C. Modelization of 3-pulse electron spin-echo decays	p. S17
Figure S12. Field dependence of T_M , ESE amplitude and frequency of the modulation in the 2-p ESE decay for [LaGd] , [GdLu] and [Gd₂]	p. S20
Figure S13. Field dependence of T_1 , ESE amplitude and frequency of the modulation in the 3-p ESE decay for [LaGd] , [GdLu] and [Gd₂]	p. S21
Figure S14. Nutation experiments for [LaGd]	p. S22
Figure S15. Nutation experiments for [GdLu]	p. S23
Figure S16. Nutation experiments for [GdLu]	p. S24

Table S1. Crystal data for compounds **[LaGd]** and **[GdLu]**.

Compound	[LaGd]	[GdLu]
Crystal size (mm ³)	0.86x0.18x0.12	0.40x0.03x0.03
Formula	C ₅₀ H ₃₄ GdLaN ₅ O ₁₉ , 5(C ₅ H ₅ N), C ₅ H ₆ N	C ₅₀ H ₃₄ GdLuN ₅ O ₁₉ , 5(C ₅ H ₅ N), C ₅ H ₆ N
FW (g mol ⁻¹)	1780.59	1816.65
Wavelength (Å)	0.71073	0.71073
Crystal system	monoclinic	monoclinic
Space group	<i>P</i> 2 ₁ / <i>n</i>	<i>P</i> 2 ₁ / <i>n</i>
<i>Z</i>	4	4
<i>T</i> (K)	100(2)	100(2)
<i>a</i> (Å)	14.4120(5)	14.268(2)
<i>b</i> (Å)	15.8616(6)	15.697(2)
<i>c</i> (Å)	32.9512(13)	33.048(4)
β (°)	90.6457(17)	92.267(5)
<i>V</i> (Å ³)	7532.1(5)	7395.8(17)
ρ_{calcd} (g cm ⁻³)	1.570	1.631
μ (mm ⁻¹)	1.513	2.398
Independent reflections	17283 (<i>R</i> _{int} = 0.0407)	8238 (<i>R</i> _{int} = 0.1345)
restraints / parameters	507 / 1068	342 / 952
Goodness-of-fit on <i>F</i> ²	1.089	1.017
Final <i>R</i> ₁ / <i>wR</i> ₂ [<i>I</i> > 2σ(<i>I</i>)]	0.0413 / 0.0501	0.0712 / 0.1564
Final <i>R</i> ₁ / <i>wR</i> ₂ [all data]	0.0903 / 0.0944	0.1150 / 0.1787
largest diff. peak and hole (e Å ⁻³)	1.789 / -1.103	1.361 / -1.330

Table S2. Metal–ligand bond distances (Å) and metal...metal separations (Å) in the structures of compounds **[LaGd]** and **[GdLu]**.

[LaGd]		[GdLu]	
La1–O6	2.466(3)	Gd1–O14	2.355(10)
La1–O14	2.482(3)	Gd1–O6	2.380(10)
La1–O1	2.492(3)	Gd1–O1	2.390(10)
La1–O13	2.543(2)	Gd1–O16	2.409(11)
La1–O8	2.583(3)	Gd1–O13	2.415(10)
La1–O16	2.648(3)	Gd1–O8	2.470(10)
La1–N2	2.648(3)	Gd1–N2	2.500(12)
La1–O3	2.701(2)	Gd1–O3	2.582(9)
La1–N1	2.757(3)	Gd1–N1	2.598(11)
La1–O17	2.796(3)		
Gd2–O4	2.357(2)	Lu2–O4	2.288(10)
Gd2–O11	2.365(3)	Lu2–O8	2.300(10)
Gd2–O8	2.381(3)	Lu2–O11	2.317(10)
Gd2–O3	2.435(2)	Lu2–O3	2.357(9)
Gd2–O19	2.438(3)	Lu2–O19	2.376(10)
Gd2–O9	2.442(3)	Lu2–O9	2.385(10)
Gd2–O13	2.448(2)	Lu2–O13	2.407(9)
Gd2–N3	2.486(3)	Lu2–N3	2.430(13)
Gd2–N5	2.687(3)	Lu2–N5	2.638(13)
Gd2...La1	3.8941(3)	Gd1...Lu2	3.7610(11)

Table S3. Details of H-bonding interactions in the structures of compounds **[LaGd]** and **[GdLu]**.

D–H...A	D–H (Å)	H...A (Å)	D–A (Å)	D–H...A (°)
[LaGd]				
O19–H19B...N1S	0.895(19)	1.92(2)	2.810(5)	177(5)
O19–H19C...N2S	0.884(19)	1.98(3)	2.809(6)	156(4)
O5–H5...O4	0.84	1.83	2.564(4)	144.5
O10–H10...O9	0.84	1.80	2.540(4)	145.8
O15–H15...O14	0.84	1.89	2.610(4)	143.1
N3S–H3...O1	0.88	1.82	2.695(5)	176.1
[GdLu]				
O19–H19C...N1S	0.91(2)	1.90(3)	2.771(19)	161(10)
O19–H19D...N2S	0.90(2)	1.90(4)	2.71(2)	149(7)
O5–H5...O4	0.84	1.91	2.553(15)	132.5
O10–H10...O9	0.84	1.78	2.530(13)	148.1
O15–H15...O14	0.84	1.98	2.670(13)	152.1
N4S–H4SB...O2	0.88	1.92	2.73(2)	152.1

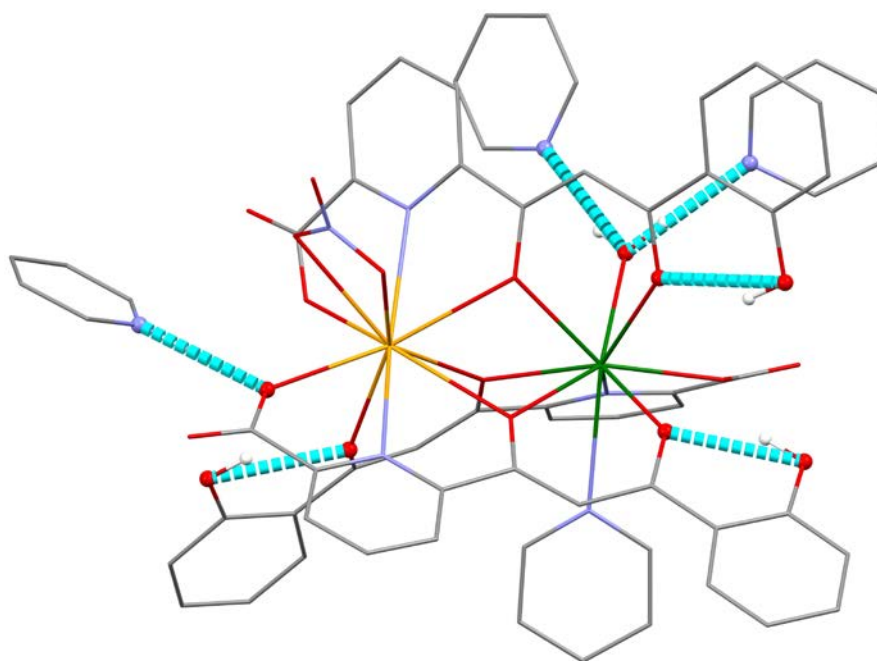


Figure S1. H-bonding in the structure of **[LaGd]**. Similar interactions are present in the structure of **[GdLu]** (see Table S3). H-bonds are depicted as thick dashed light blue lines. Only atoms involved in H-bonds are shown as balls. Colour code: O, red; N, light blue; H, white; C, grey; La, orange; Gd, green.

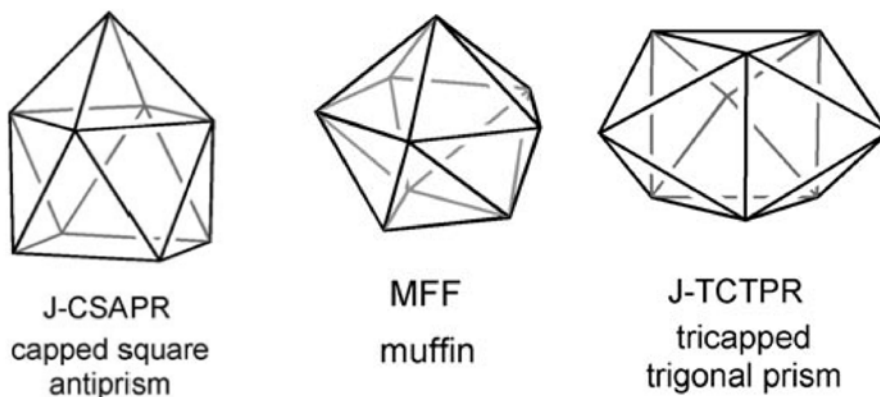


Figure S2. Ideal nine-vertex polyhedral to which the coordination geometry of the Gd(III) ions in [LaGd], [GdLu] and [Gd₂] are compared through Continuous shape measures: capped square antiprism, muffin and tricapped trigonal prism. Calculated distances to these ideal polyhedral are:

Gd2 in [LaGd]: **0.657** to **TCTPR**, **0.701** to **CSAPR** and 1.223 to MFF

Gd1 in [GdLu]: **3.010** to **MFF**, 4.132 to CSAPR and 4.782 to TCTPR

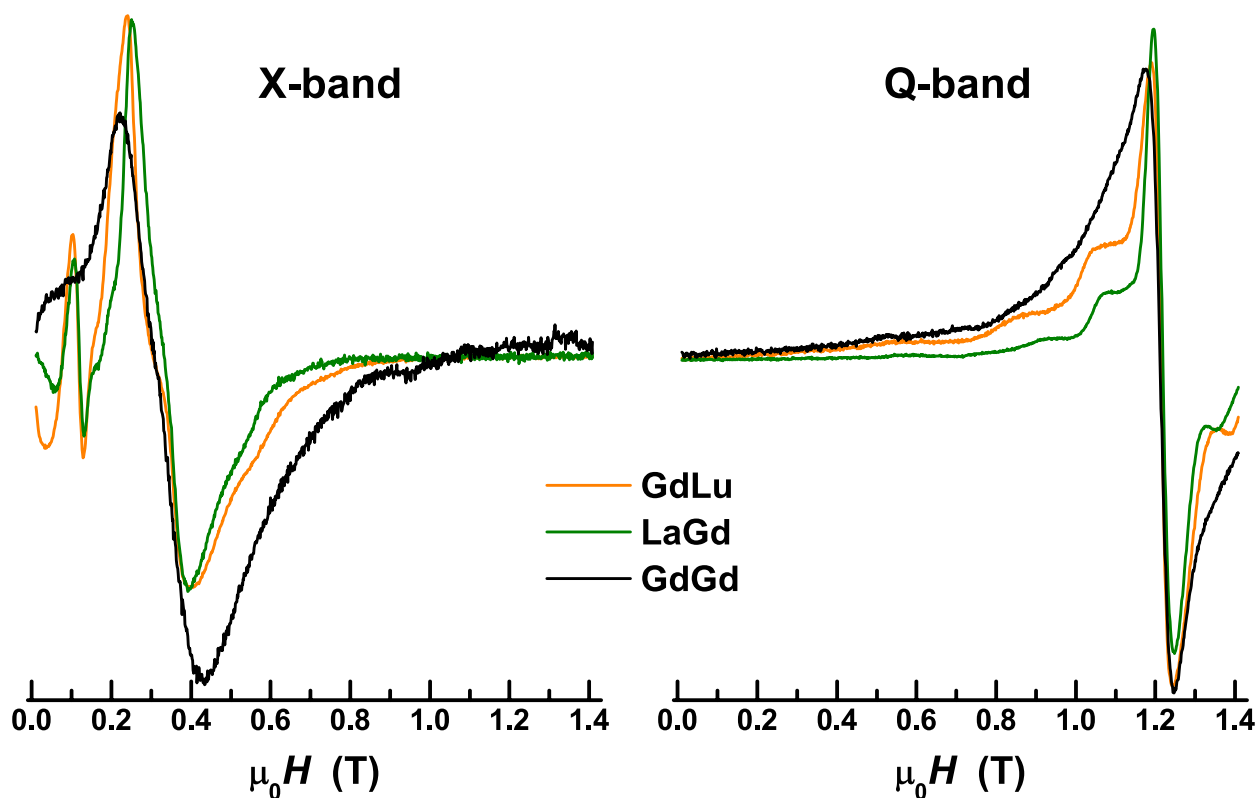


Figure S3. X-band and Q-band cw-ESR spectra of polycrystalline samples of **[LaGd]**, **[GdLu]** and **[Gd₂]** as indicated. The positions of the absorption derivative maxima and minima show that spectra measured on the latter compound are not simple superpositions of those measured on the former two, the difference being more visible at lower magnetic fields (X-band).

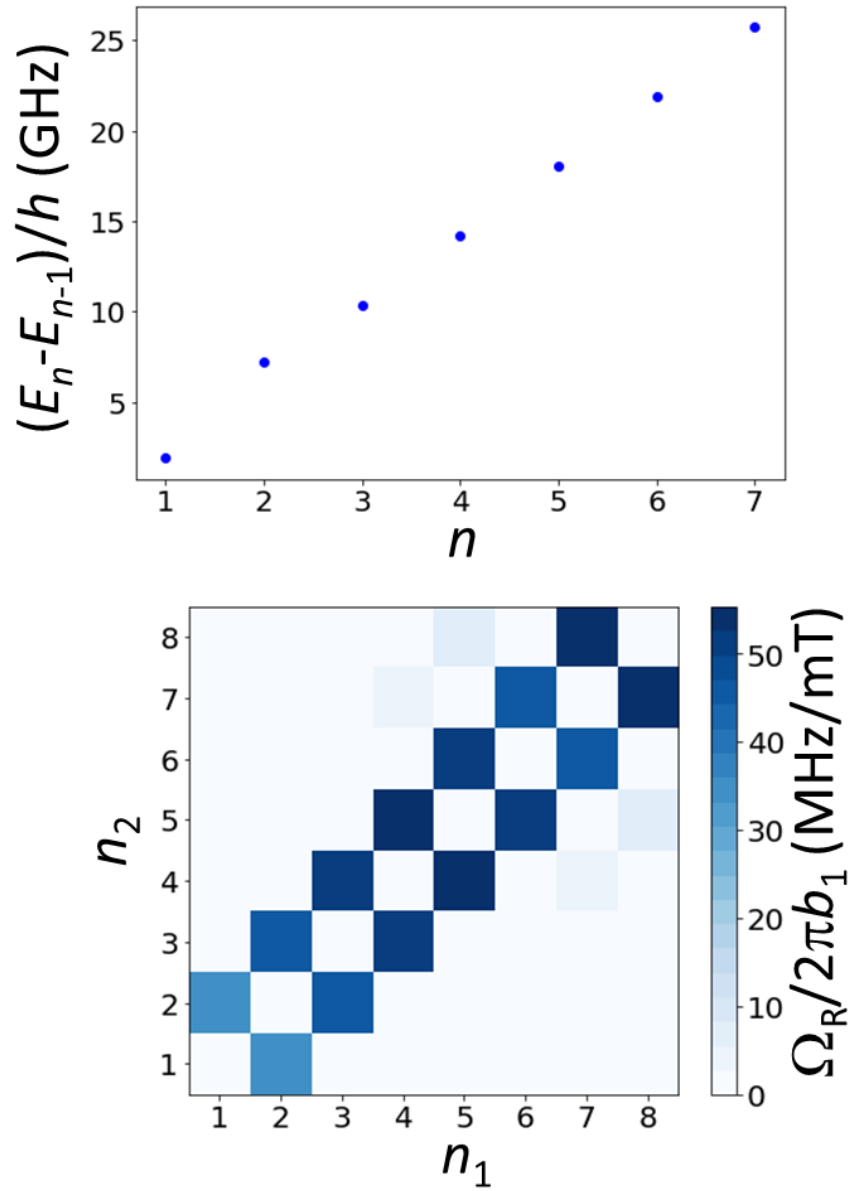


Figure S4. Top: Transition frequencies between adjacent levels $n-1$ and n of **[LaGd]** calculated at $\mu_0 H_z = 0.5$ T. Bottom: Rabi frequencies for resonant transitions between different spin states of **[LaGd]**, calculated at $\mu_0 H_z = 0.5$ T.

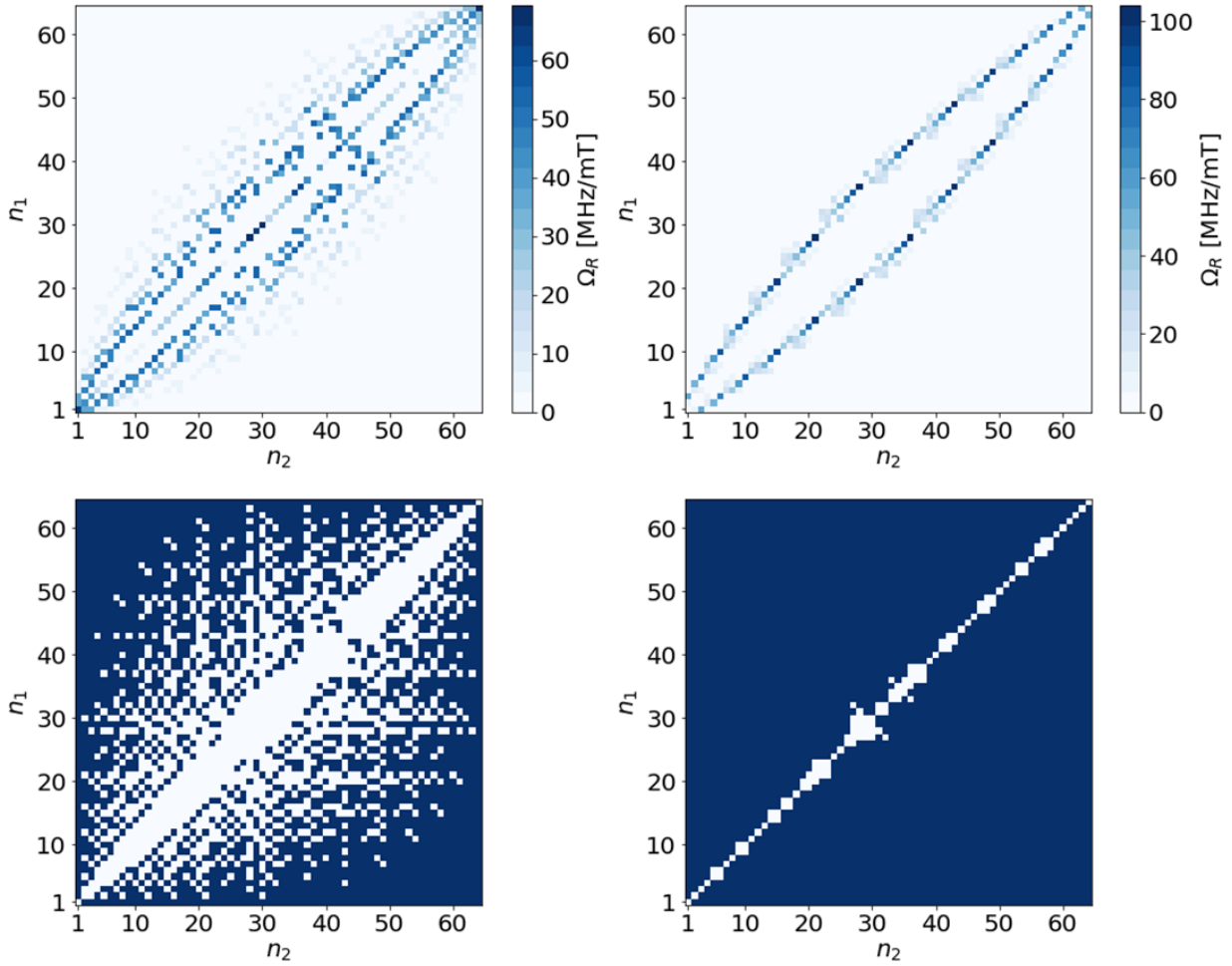


Figure S5. Two methods to break universality in a pair of $S = 7/2$ qubits, to be compared with Fig. 7 of the main text. Top: Colour map of the Rabi frequencies calculated with Eq. (2) of the main text and the magnetic anisotropy constants of **[Gd₂]** at $\mu_0 H = 0.5$ T and $J = 0$, i.e. for uncoupled spins (left) and at $\mu_0 H = 10$ T and $J = -0.02$ K (right), i.e. for a magnetic field stronger than the magnetic anisotropy and the spin-spin coupling. Bottom: transitions (in blue dark) attainable by concatenating resonant transitions having $\Omega_R/b_1 > 0.2$ MHz/mT. The white spots signal unfeasible gates.

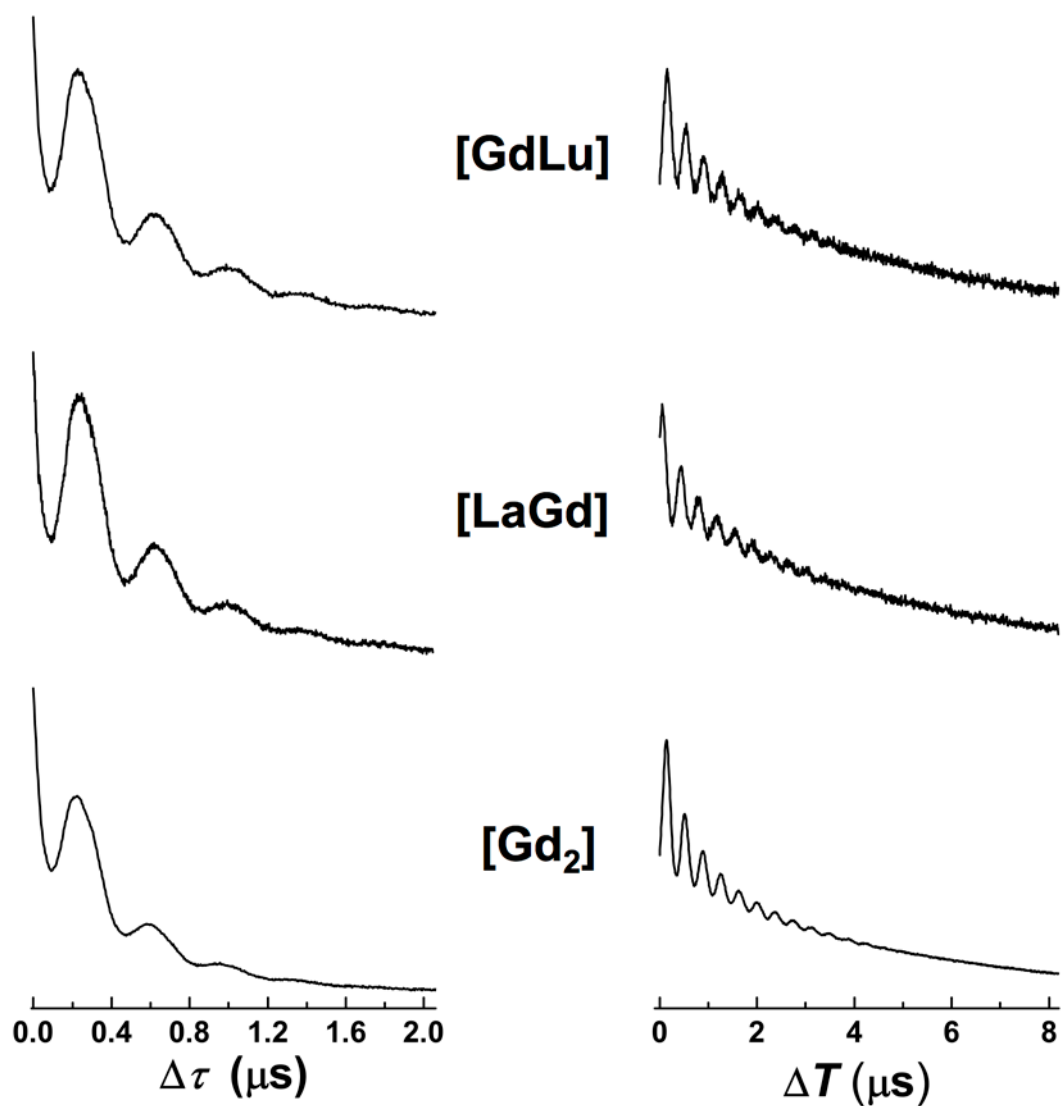


Figure S6. Representative 2-pulse (left, $\mu_0H = 400$ mT) and 3-pulse (right, $\mu_0H = 410$ mT) electron spin-echo decay for **[LaGd]**, **[GdLu]** and **[Gd₂]** as indicated. All data collected at 6 K on frozen diluted MeOH-d⁴:EtOH-d⁶ solutions.

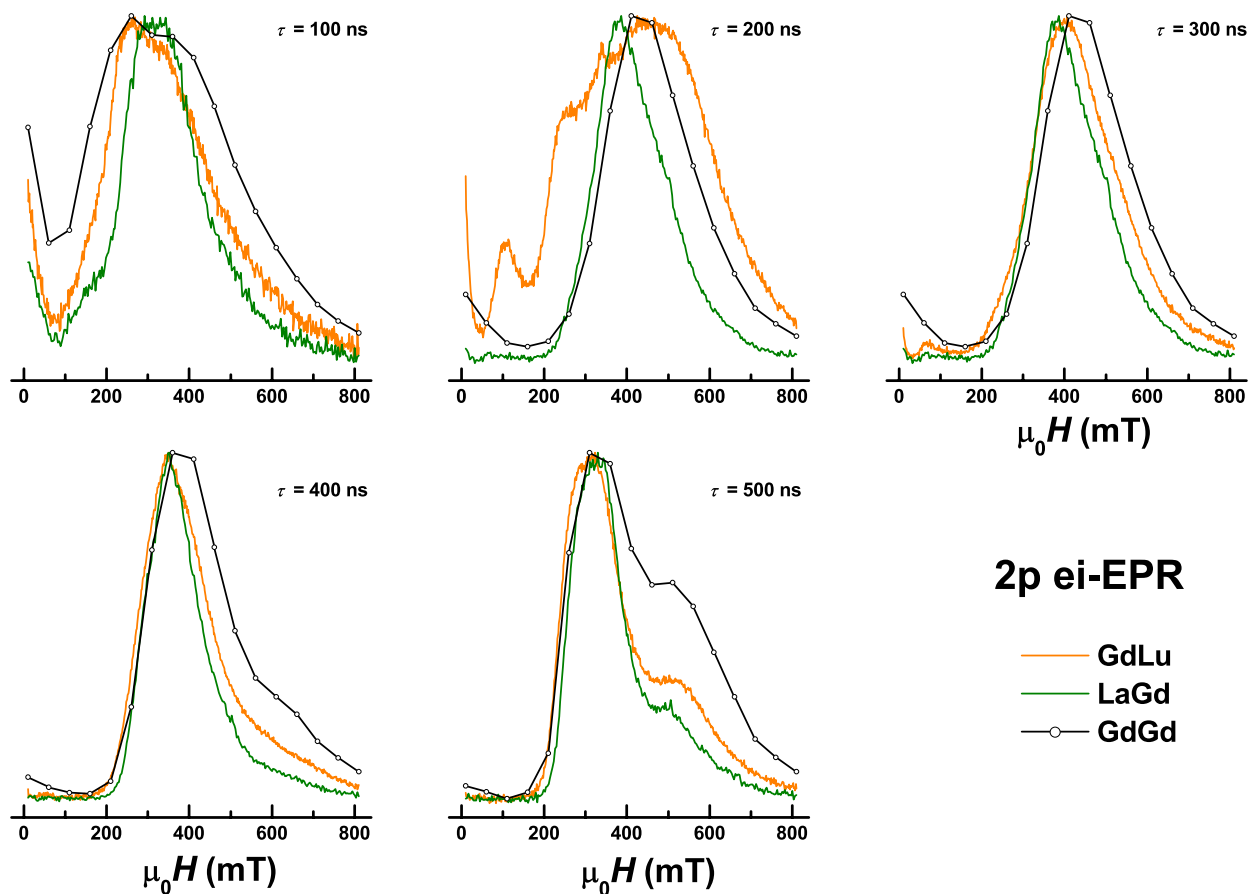


Figure S7. Echo-induced EPR spectra for [LaGd], [GdLu] and [Gd₂] as derived from 2-pulse experiments and varying τ , as indicated. All data collected at 6 K on frozen diluted MeOH-d⁴:EtOH-d⁶ solutions.

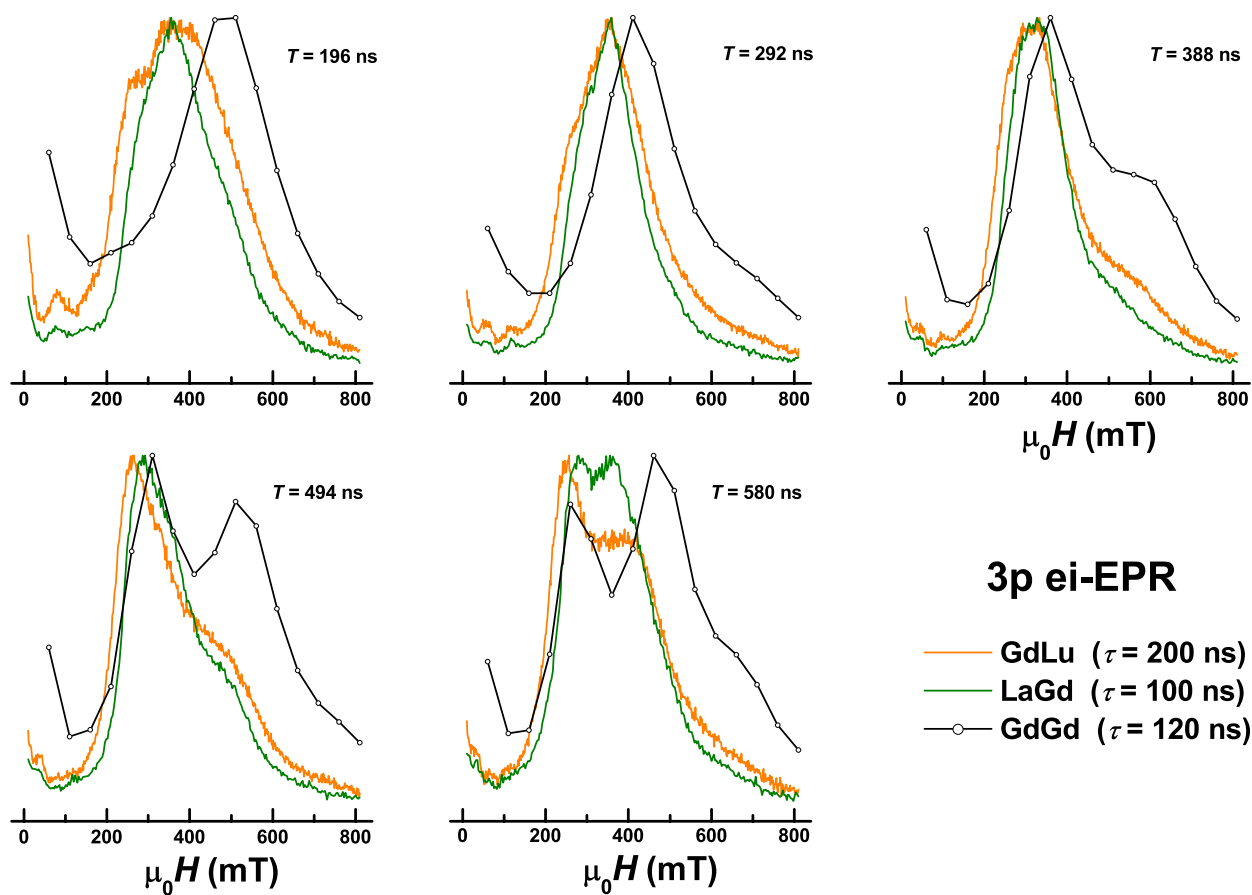


Figure S8. Echo-induced EPR spectra for [LaGd], [GdLu] and [Gd₂] as derived from 3-pulse experiments and varying T , as indicated. All data collected at 6 K on frozen diluted MeOH-d⁴:EtOH-d⁶ solutions.

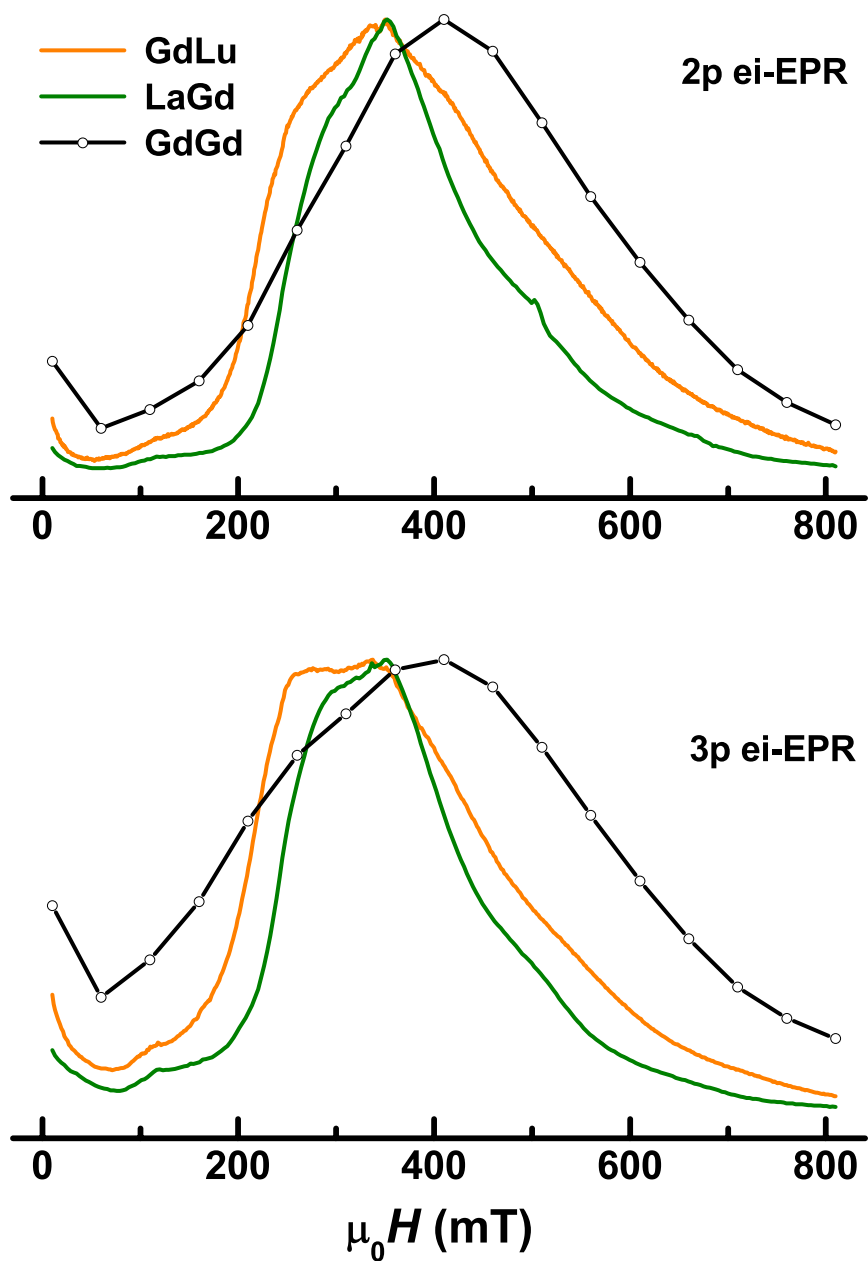


Figure S9. Echo-induced EPR spectra for [LaGd], [GdLu] and [Gd₂] as derived from 2-pulse (top) and 3-pulse (bottom) experiments and summing for all τ and T, as indicated. All data collected at 6 K on frozen diluted MeOH-d⁴:EtOH-d⁶ solutions.

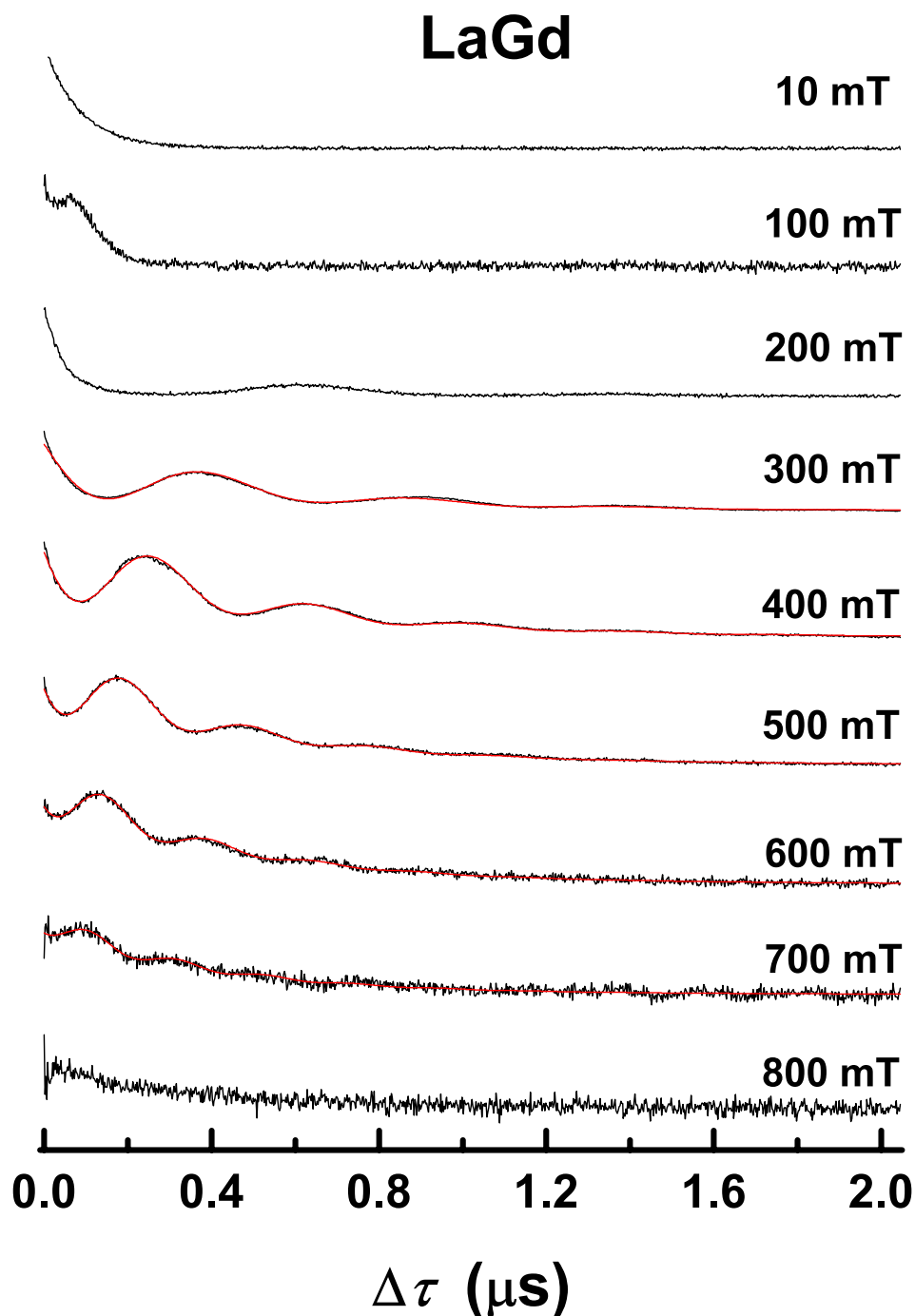


Figure S10A. 2-pulse electron spin-echo decay at the indicated magnetic fields μ_0H for [LaGd]. Full red lines correspond to the best-fit to the equation

$$y(\tau) = y_0 + A_{2p} e^{-2\tau/T_M} \{1 + k e^{-\lambda\tau} \cos(2\pi\nu\tau + \phi)\}$$

in which y_0 is background, A_{2p} the initial amplitude, T_M the phase memory time, k the relative amplitude of the modulated signal, λ the additional decay of the oscillating component and ν its frequency and ϕ the non-zero phase due to the detector dead-time. All data collected at 6 K on frozen diluted MeOH-d⁴:EtOH-d⁶ solutions.

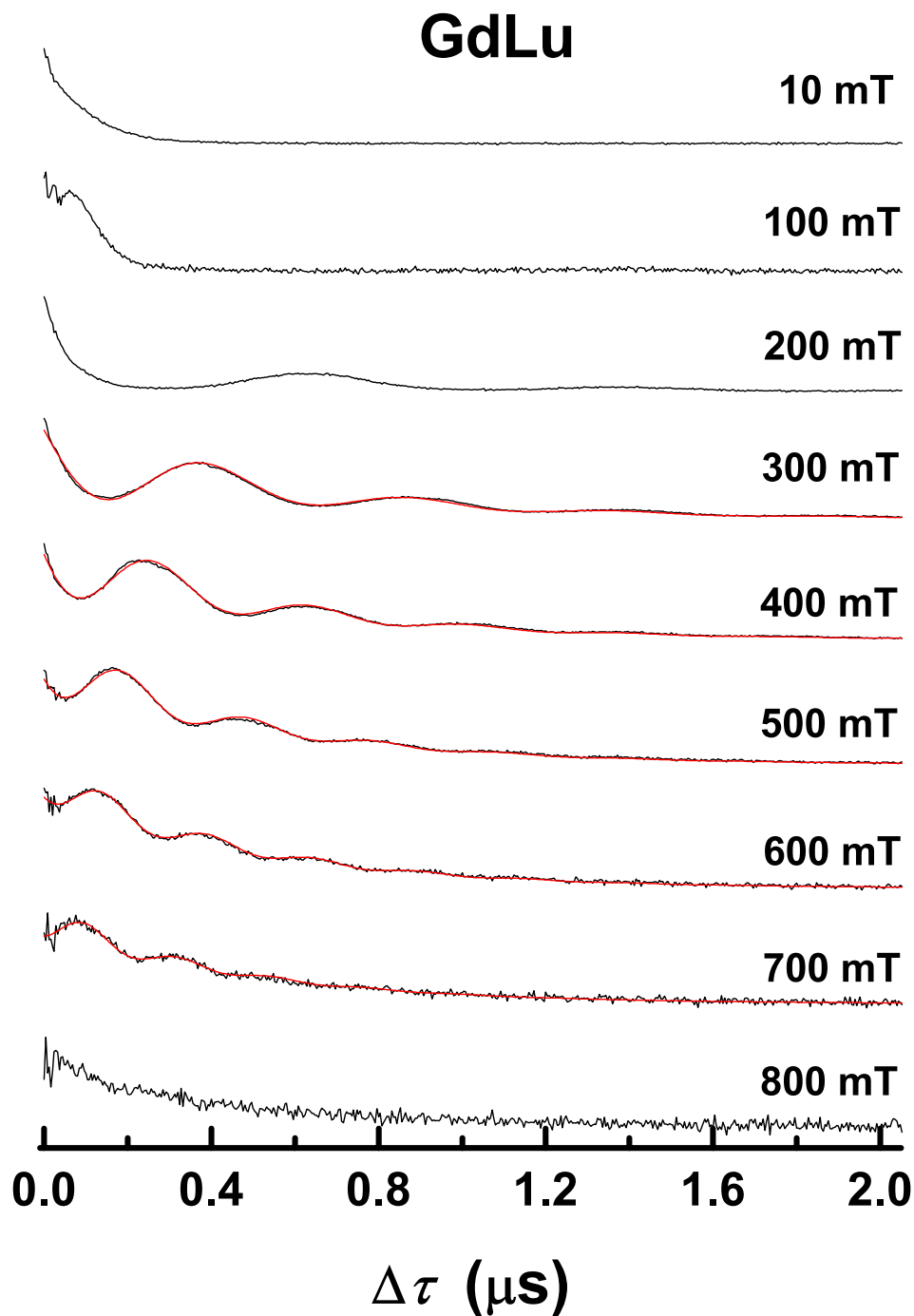


Figure S10B. 2-pulse electron spin-echo decay at the indicated magnetic fields μ_0H for [GdLu]. Full red lines correspond to the best-fit to the equation

$$y(\tau) = y_0 + A_{2p} e^{-2\tau/T_M} \{1 + k e^{-\lambda\tau} \cos(2\pi\nu\tau + \phi)\}$$

in which y_0 is background, A_{2p} the initial amplitude, T_M the phase memory time, k the relative amplitude of the modulated signal, λ the additional decay of the oscillating component and ν its frequency and ϕ the non-zero phase due to the detector dead-time. All data collected at 6 K on frozen diluted MeOH-d⁴:EtOH-d⁶ solutions.

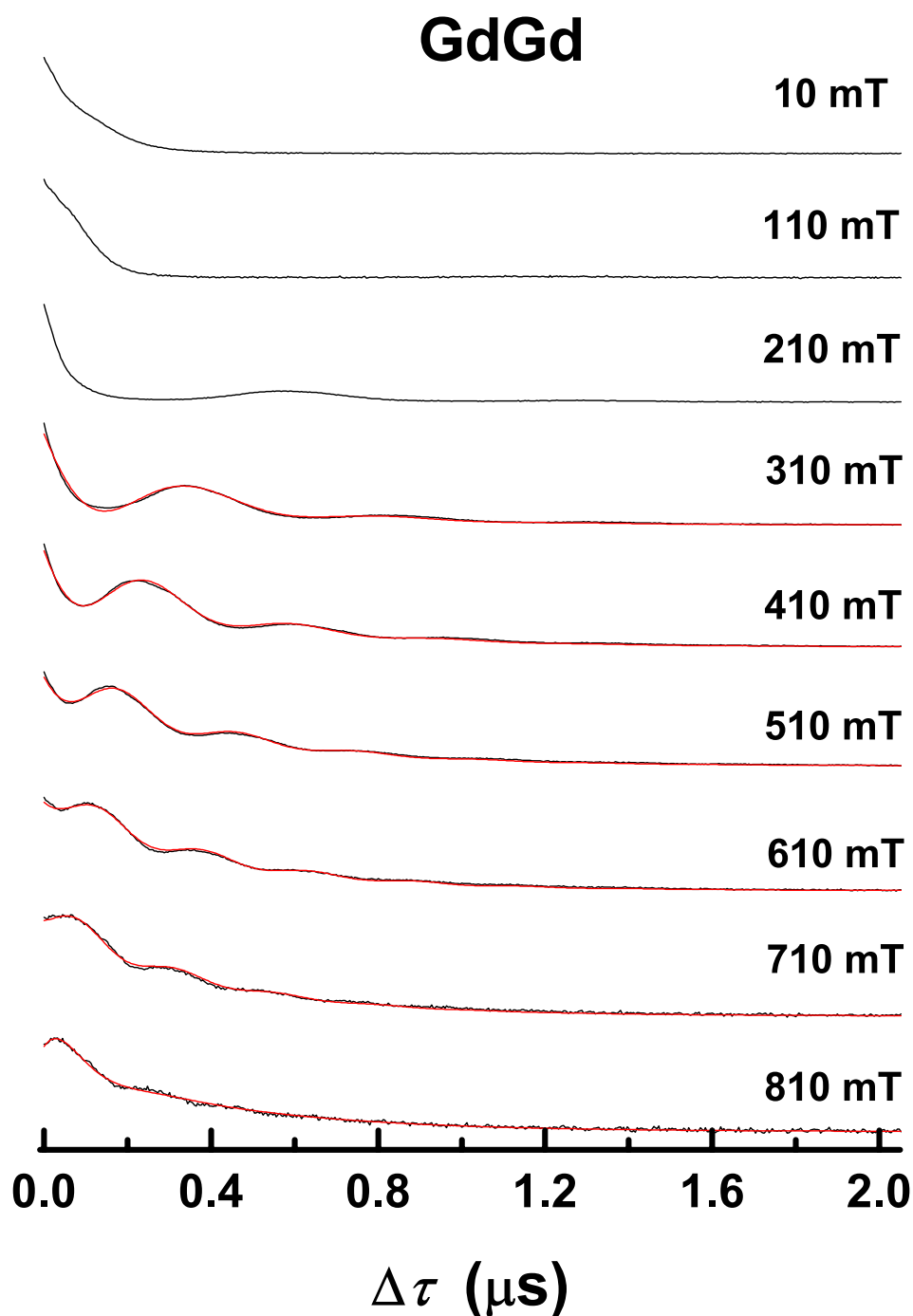


Figure S10C. 2-pulse electron spin-echo decay at the indicated magnetic fields μ_0H for **[GdGd]**. Full red lines correspond to the best-fit to the equation

$$y(\tau) = y_0 + A_{2p} e^{-2\tau/T_M} \{1 + k e^{-\lambda\tau} \cos(2\pi\nu\tau + \phi)\}$$

in which y_0 is background, A_{2p} the initial amplitude, T_M the phase memory time, k the relative amplitude of the modulated signal, λ the additional decay of the oscillating component and ν its frequency and ϕ the non-zero phase due to the detector dead-time. All data collected at 6 K on frozen diluted MeOH- d^4 :EtOH- d^6 solutions.

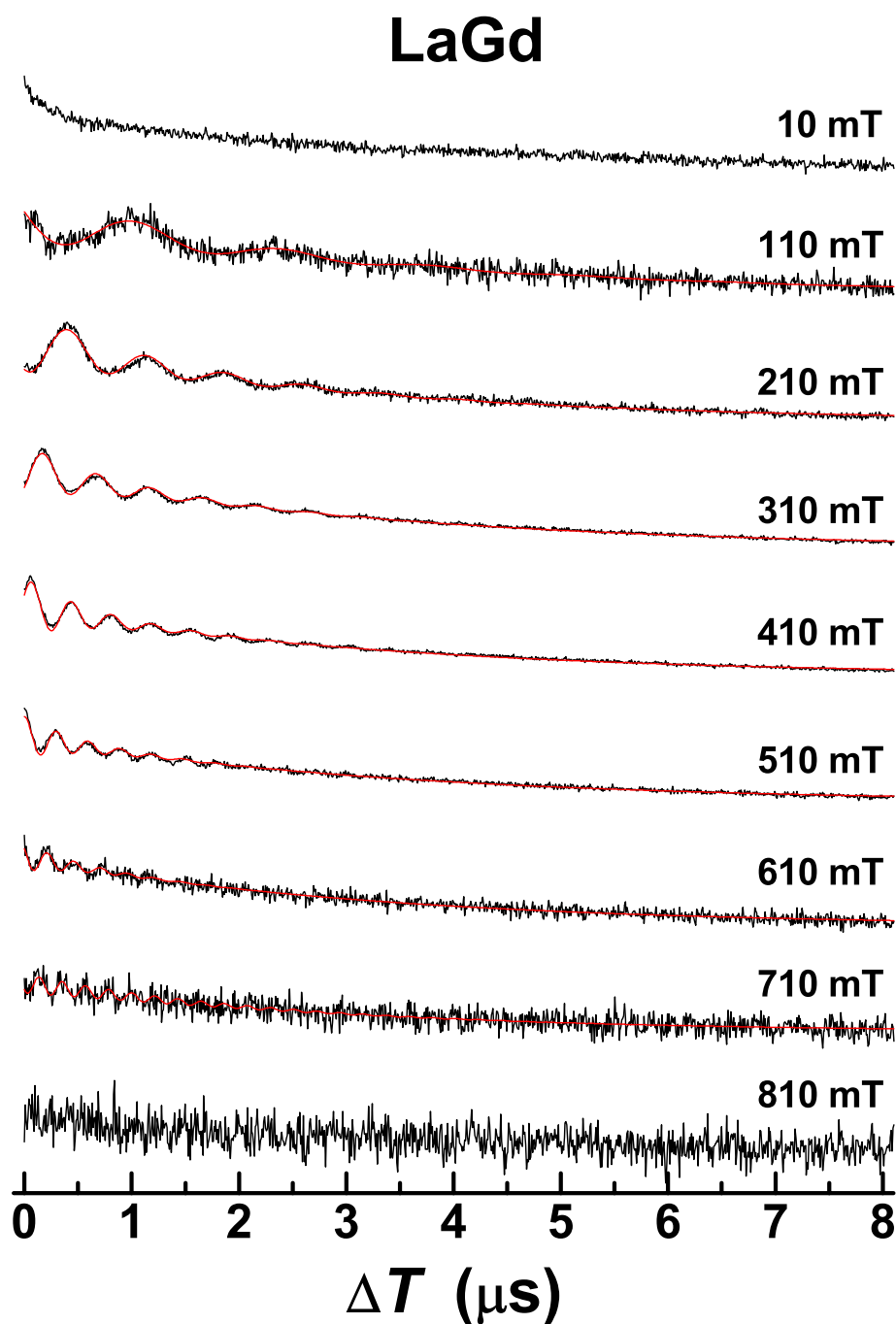


Figure S11A. 3-pulse electron spin-echo decay at the indicated magnetic fields $\mu_0 H$ for [LaGd]. Full red lines correspond to the best-fit to the equation

$$y(\tau) = y_0 + A_{3p} e^{-\tau/T_1} \{1 + k e^{-\lambda\tau} \cos(2\pi\nu\tau + \phi)\}$$

in which y_0 is background, A_{3p} the initial amplitude, T_1 the spin-relaxation time, k the relative amplitude of the modulated signal, λ the additional decay of the oscillating component and ν its frequency and ϕ the non-zero phase due to the detector dead-time. All data collected at 6 K on frozen diluted MeOH- d^4 :EtOH- d^6 solutions.

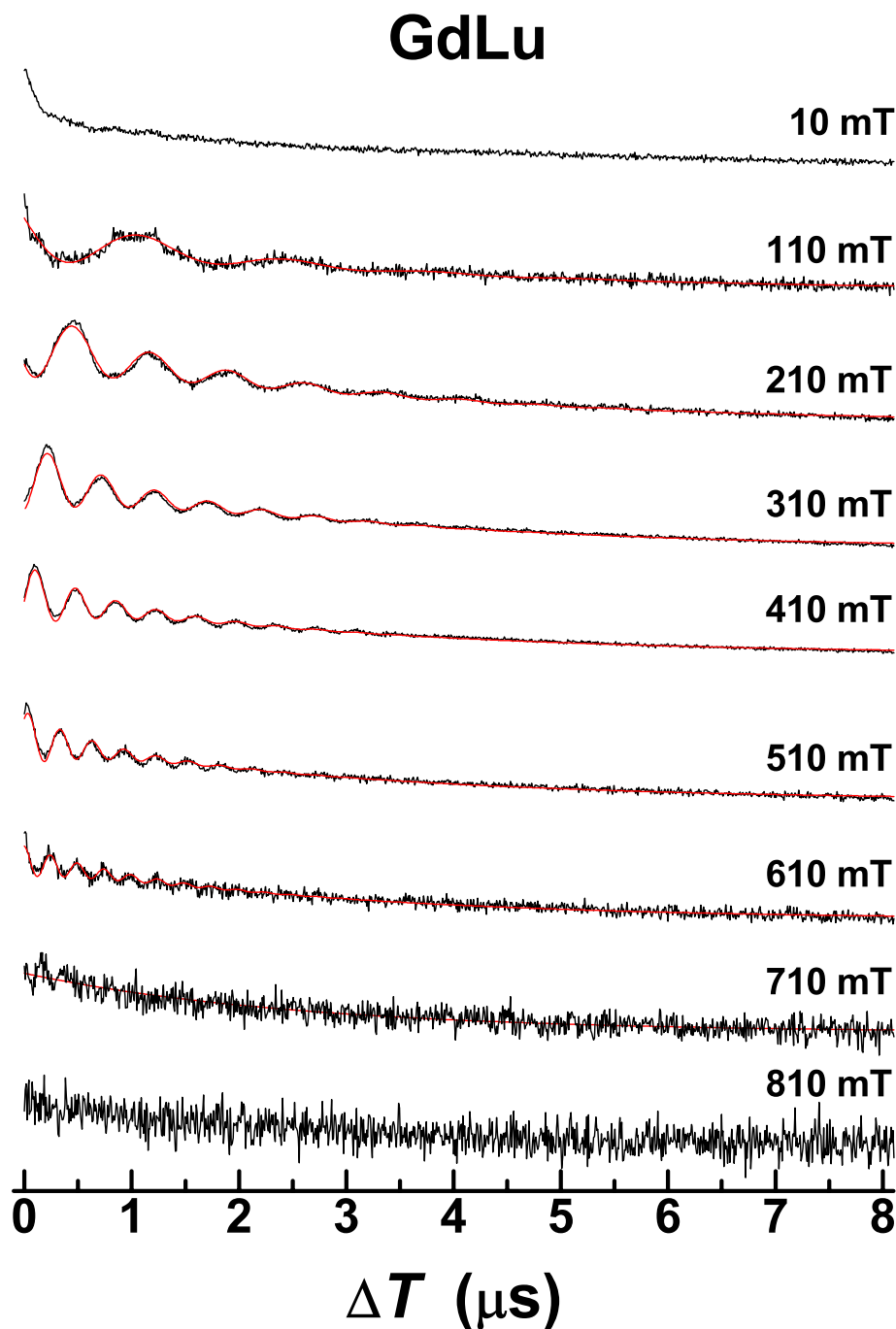


Figure S11B. 3-pulse electron spin-echo decay at the indicated magnetic fields $\mu_0 H$ for [GdLu]. Full red lines correspond to the best-fit to the equation

$$y(\tau) = y_0 + A_{3p} e^{-\tau/T_1} \{1 + k e^{-\lambda\tau} \cos(2\pi\nu\tau + \phi)\}$$

in which y_0 is background, A_{3p} the initial amplitude, T_1 the spin-relaxation time, k the relative amplitude of the modulated signal, λ the additional decay of the oscillating component and ν its frequency and ϕ the non-zero phase due to the detector dead-time. All data collected at 6 K on frozen diluted MeOH-d⁴:EtOH-d⁶ solutions.

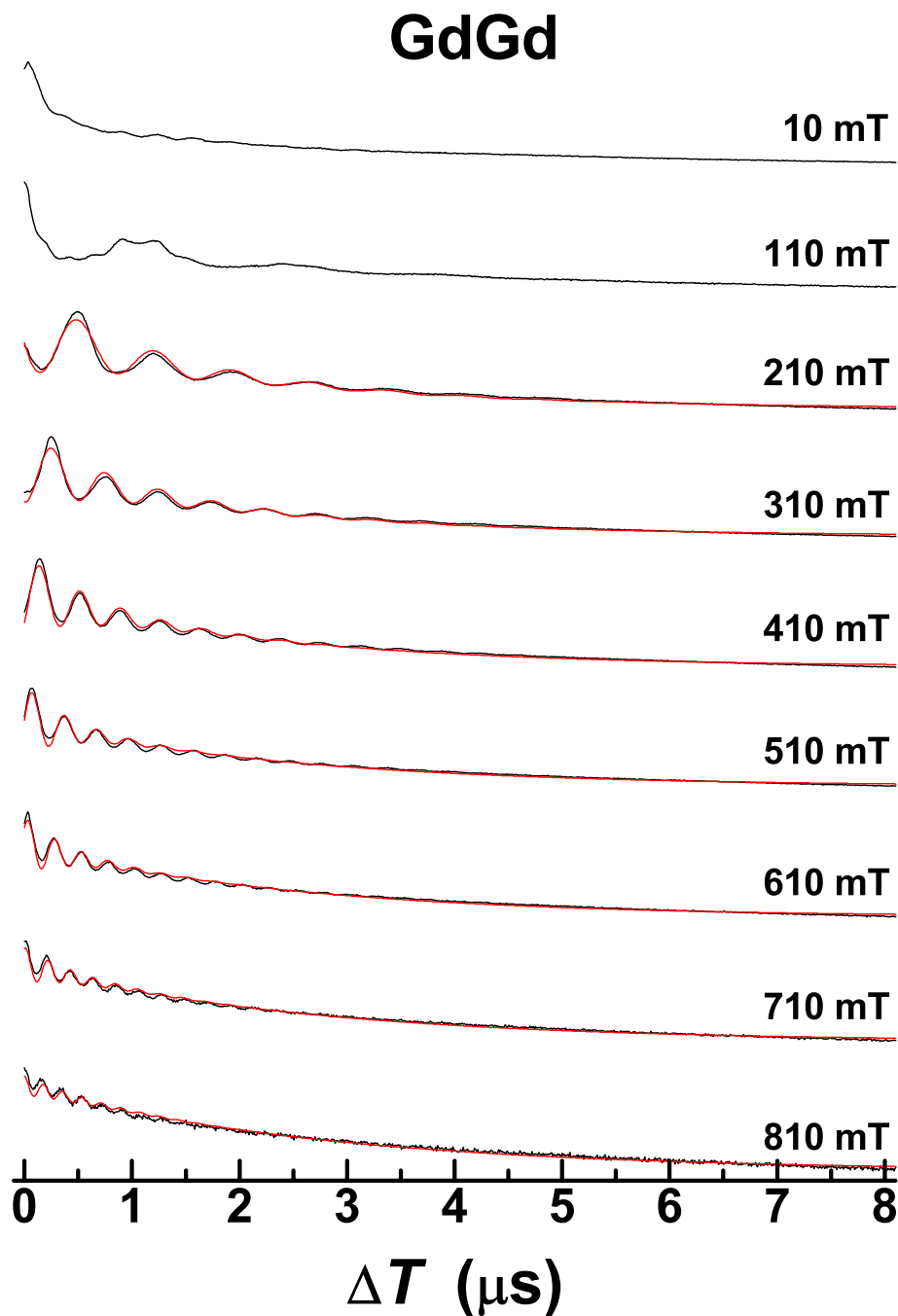


Figure S11C. 3-pulse electron spin-echo decay at the indicated magnetic fields $\mu_0 H$ for **[GdGd]**. Full red lines correspond to the best-fit to the equation

$$y(\tau) = y_0 + A_{3p} e^{-\tau/T_1} \{1 + k e^{-\lambda\tau} \cos(2\pi\nu\tau + \phi)\}$$

in which y_0 is background, A_{3p} the initial amplitude, T_1 the spin-relaxation time, k the relative amplitude of the modulated signal, λ the additional decay of the oscillating component and ν its frequency and ϕ the non-zero phase due to the detector dead-time. All data collected at 6 K on frozen diluted MeOH-d⁴:EtOH-d⁶ solutions.

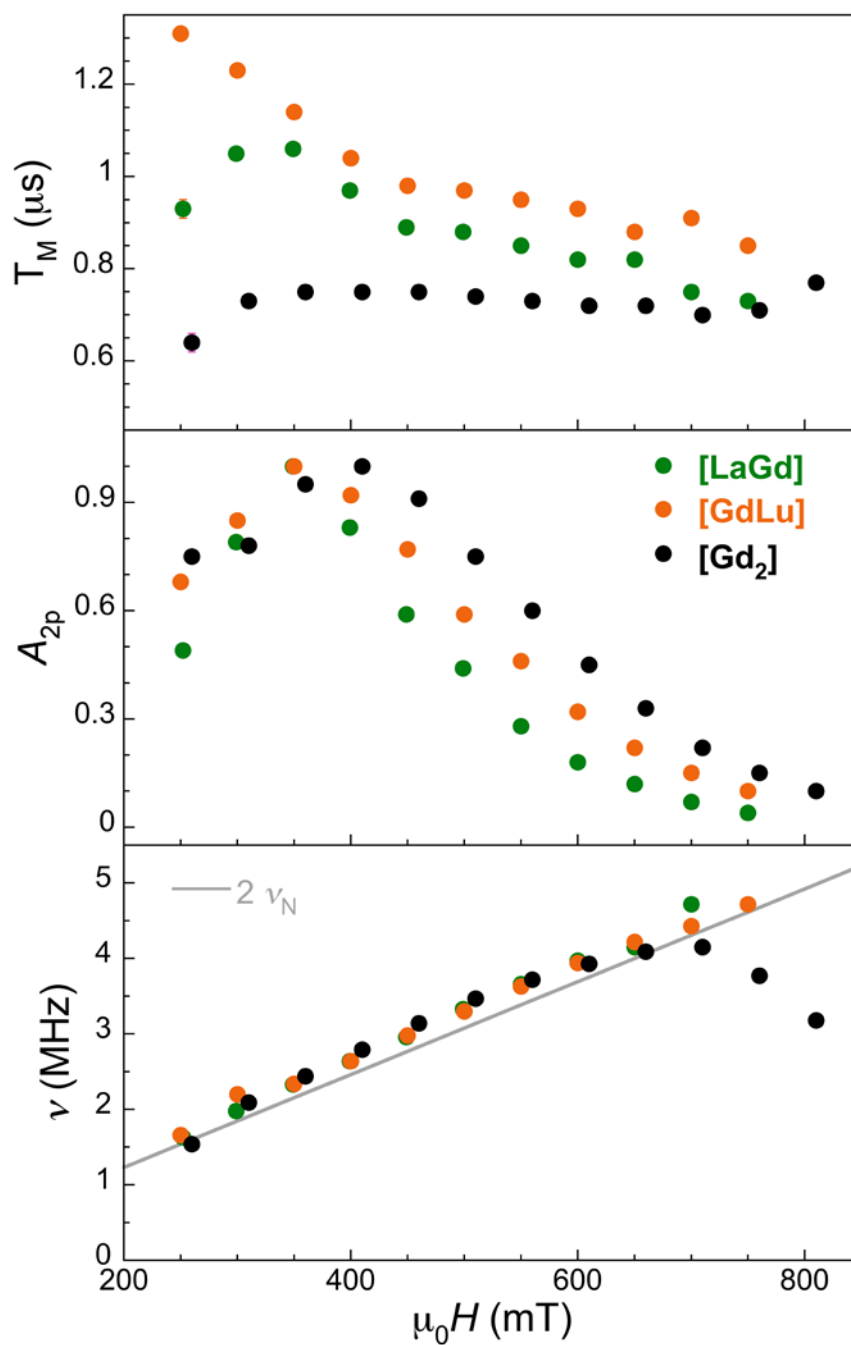


Figure S12. Comparison of the field dependence of the phase memory time T_M (top), ESE amplitude (middle) and frequency of the modulation in the ESE decay ν (bottom) derived for diluted MeOH- d^4 :EtOH- d^6 solutions of [LaGd], [GdLu] and [Gd₂] at 6 K from simulation of 2-pulse ESE decays. The full grey line (bottom) depicts the field dependence of twice the Larmor frequency of the ¹⁴N nucleus.

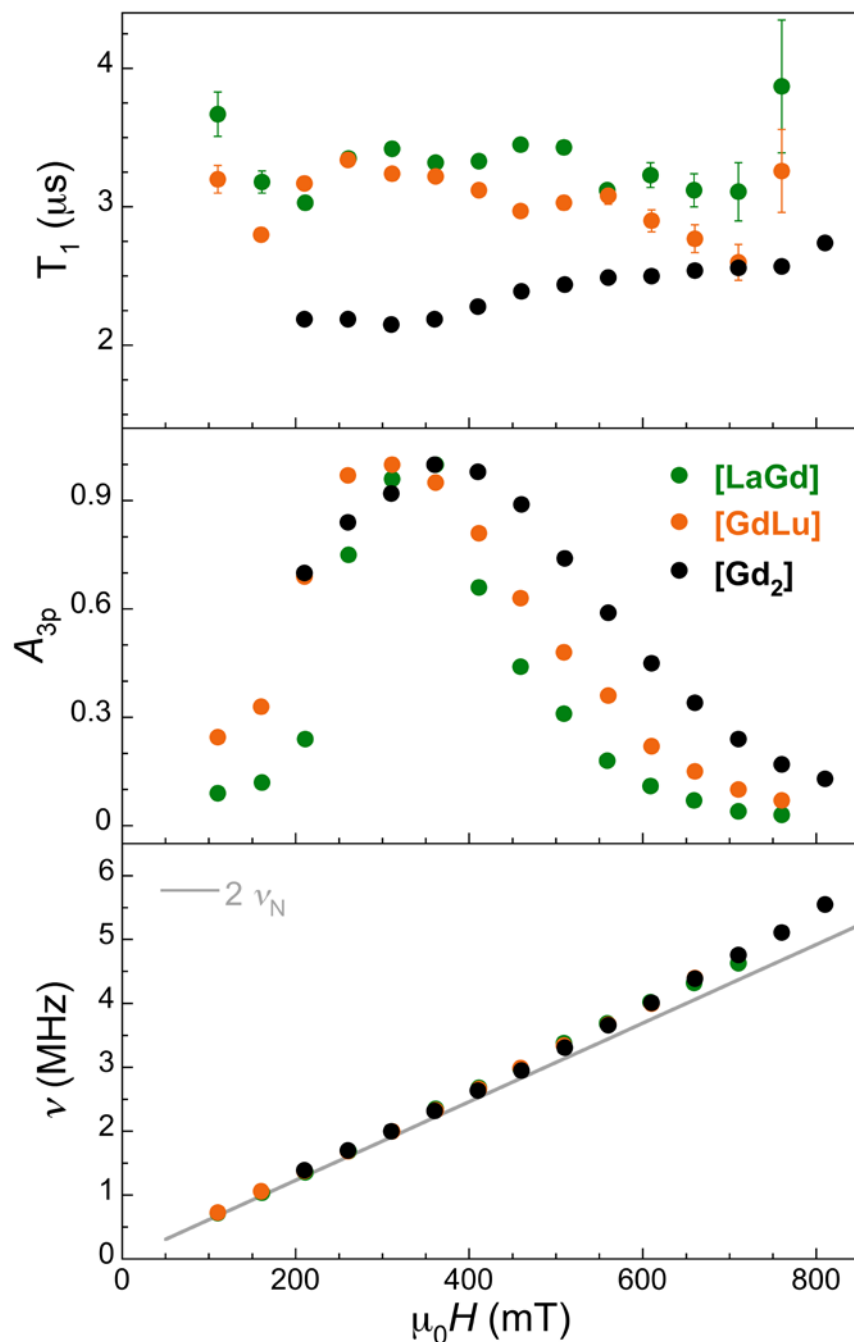


Figure S13. Comparison of the field dependence of the spin-lattice relaxation T_1 (top), ESE amplitude (middle) and frequency of the modulation in the ESE decay ν (bottom) derived for diluted MeOH- d^4 :EtOH- d^6 solutions of [LaGd], [GdLu] and [Gd₂] at 6 K from simulation of 3-pulse ESE decays. The full grey line (bottom) depicts the field dependence of twice the Larmor frequency of the ^{14}N nucleus.

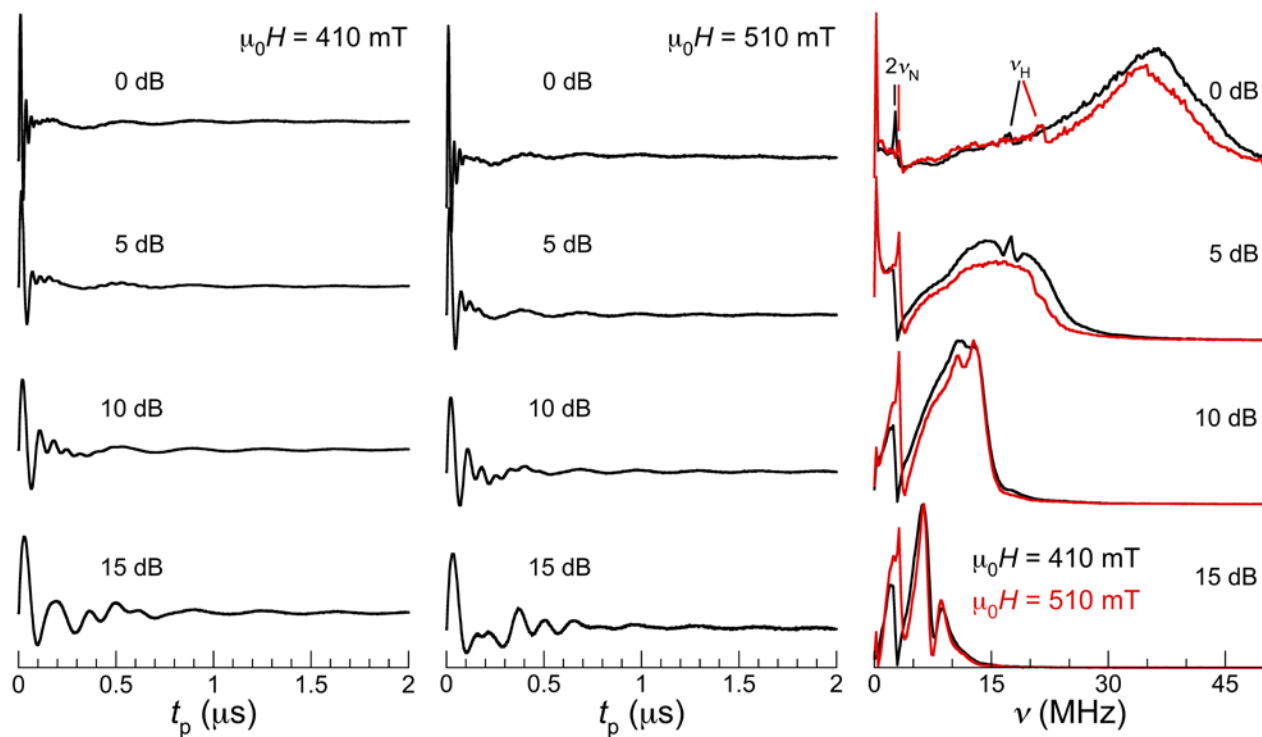


Figure S14. Nutation experiments measured on a diluted MeOH- d^4 :EtOH- d^6 solution of [LaGd] at 6 K and $\mu_0 H = 410$ (left) and 510 (middle) mT. Right: Normalised Fourier Transforms showing the main Rabi frequency and revealing additional oscillations with characteristic frequencies that correspond to twice the Larmor frequency of ^{14}N and to the Larmor frequency of ^1H , as indicated.

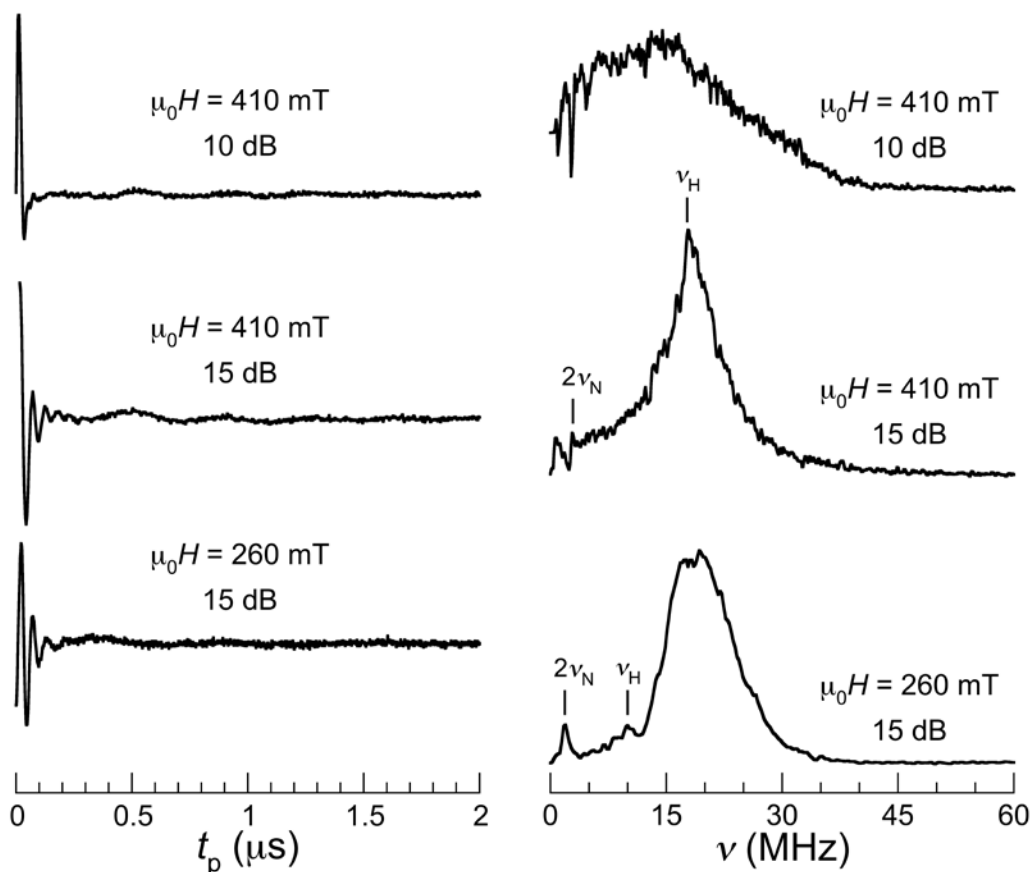


Figure S15. Left: Nutation experiments measured on a diluted MeOH-d⁴:EtOH-d⁶ solution of **[GdLu]** at 6 K and $\mu_0 H = 410$ (10 and 15 dB) and 260 (15 dB) mT. Right: Corresponding Fourier Transforms showing the main Rabi frequency and revealing additional oscillations with characteristic frequencies that correspond to twice the Larmor frequency of ¹⁴N and to the Larmor frequency of ¹H, as indicated. Fourier transformations.

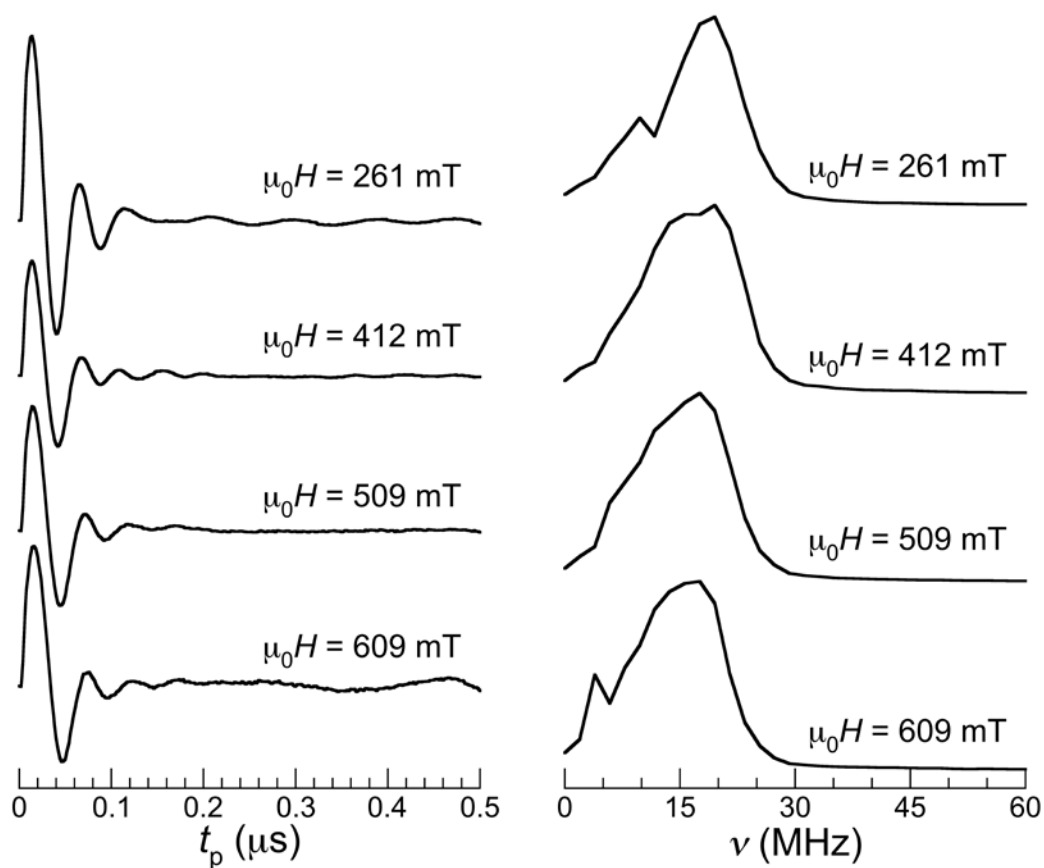


Figure S16. Left: Nutation experiments measured on a diluted MeOH-d⁴:EtOH-d⁶ solution of **[GdLu]** at 6 K and increasing fields $\mu_0 H$ as indicated. Right: Corresponding Fourier Transforms showing the main Rabi frequency.

Note that because these measurements were done with a lower resolution (256 points and a smaller interval of 2 ns), the frequency resolution is $\Delta\nu = 1.95$ MHz, thus not allowing to observe with confidence the possible characteristic frequencies corresponding to twice the Larmor frequency of ¹⁴N and to the Larmor frequency of ¹H.